Design of LRRK2 inhibitors using a CHK1-derived crystallographic surrogate

Douglas S. Williamson,[†] Garrick P. Smith,[‡] Pamela Acheson-Dossang,[†] Simon T. Bedford,[†] Victoria Chell,[†] I-Jen Chen,[†] Justus C. A. Daechsel,[‡] Zoe Daniels,[†] Laurent David,[‡] Pawel Dokurno,[†] Morten Hentzer,[‡] Martin C. Herzig,[‡] Roderick E. Hubbard,[†] Jonathan D. Moore,[†] James B. Murray,[†] Samantha Newland,[†] Stuart C. Ray,[†] Terry Shaw,[†] Allan E. Surgenor,[†] Lindsey Terry,[†] Kenneth Thirstrup,[†] Yikang Wang[†] and Kenneth V. Christensen[‡]*

[†]Vernalis (R&D) Ltd, Granta Park, Great Abington, Cambridge, CB21 6GB, United Kingdom

[‡]H. Lundbeck A/S, Ottiliavej 9, 2500 Valby, Denmark

KEYWORDS: Parkinson's disease, PD, leucine-rich repeat kinase 2, LRRK2, kinase inhibitor, checkpoint kinase 1, CHK1, mutant, CHK1 10-pt. mut., surrogate, pyrrolo[2,3-*b*]pyridine

Mutations in leucine-rich repeat kinase 2 (LRRK2), such as G2019S, are associated with an increased risk of developing Parkinson's disease. A CHK1-derived LRRK2 G2019S kinase domain surrogate was obtained and validated by comparing its affinity with LRRK2 inhibitors and their LRRK2 G2019S activity. X-ray crystal structures of the surrogate with known LRRK2

inhibitors rationalized their potency and selectivity. Fragment hit-derived arylpyrrolo[2,3-*b*]-pyridine LRRK2 inhibitors underwent surrogate structure-guided optimization. LRRK2-pSer935 HEK293 IC_{50} for **22** on LRRK2 WT and its G2019S and A2016T mutants was 24 nM, 40 nM and 471 nM, respectively. Cellular data for **22** were consistent with binding to Ala2016 in LRRK2 (equivalent to Ala147 in CHK1 10-pt. mut. structure). **22** was shown to be potent, selective, orally available and brain-penetrant in wild-type mice, and confirmation of target engagement was demonstrated, with LRRK2-pSer935 IC_{50} values for **22** in mouse brain and kidney being 1.3 nM and 5 nM, respectively.

INTRODUCTION

Parkinson's disease (PD) is a neurodegenerative disorder typically characterized by motor symptoms of resting tremor, slowness of movement and muscular rigidity, as well as non-motor symptoms such as pain and depression.[1] Pathologically, the disease is identified by the loss of dopaminergic neurons, with a consequent decrease in dopamine levels in the brain and by aggregation of the protein α-synuclein in the dopaminergic neurons. These aggregations, known as Lewy bodies, are composed of insoluble α-synuclein, associated with other proteins such as ubiquitin.[2] Current PD therapies aim at increasing the dopamine levels in areas innervated by dopaminergic neurons in the brain; none, however, address the underlying disease-causing problem. Many alternative approaches to treating PD are therefore under investigation,[3,4] one of which is inhibition of leucine-rich repeat kinase 2 (LRRK2).

LRRK2 is a 2527 amino acid, multi-domain protein involved in catalyzing phosphorylation and GTP-GDP hydrolysis.[5,6,7,8] Evidence showing a relationship between LRRK2 and the

pathogenesis of PD is mounting.[9,10] It has been shown that LRRK2 phosphorylates α-synuclein at Ser129, and this phosphorylated form constitutes a significant part of Lewy bodies.[11] Additionally, single nucleotide polymorphisms in the functional domains of LRRK2 have been associated with familial and sporadic Parkinson's disease.[12] Importantly, the clinical features of PD associated with LRRK2 mutations cannot be distinguished from those featuring in idiopathic PD.[13] This strongly suggests a common pathogenic mechanism, and that LRRK2 activity is a rate-limiting factor in PD progression.[14]

Several LRRK2 pathogenic variants have been identified in PD patients,[15] most commonly the G2019S substitution in the activation loop of the kinase domain of the protein.[16] G2019S PD is inherited in an autosomal dominant fashion, suggesting a gain-of-function mutation of the LRRK2 protein.[17] In support of this hypothesis, biochemical studies on G2019S, as well as I2020T mutants, showed increased kinase activity of LRRK2.[18] This suggests a causal involvement of overactive LRRK2 in the pathogenesis of familial forms of PD. Thus, inhibitors of LRRK2, including the G2019S mutation, could be used as disease modifying treatment in familial PD.[19,20,21,22,23,24,25,26,27,28,29,30]

LRRK2 kinase domain inhibitors previously reported (Figure 1) range from broad spectrum kinase inhibitors such as staurosporine **1**,[31] to more selective inhibitors such as aminopyrimido-benzodiazepinone **2** (LRRK2-IN-1),[32] which have poor CNS penetration. Further efforts have led to the discovery of CNS penetrant, selective inhibitors such as arylbenzamide **3a** (GSK2578215A),[33] aminopyrimidine **4a** (GNE-7915),[34] pyrrolopyrimidines **5** (PF-06447475)[35] and **6** (JH-II-127),[36] indazole **7** (MLi-2),[37,38] and aminopyridine **8**.[39] There has not yet, however, been a report on the progression of a compound into the clinic, which would require sufficient target engagement, and an acceptable pharmacokinetic and safety profile.[40,41]

The design of LRRK2 inhibitors has been impeded in part by the complexity of this large multi-domain protein, such that stable, soluble, crystallizable kinase domain constructs have not yet been obtained.[42] Discovery efforts have primarily used homology models based on other kinases with similar sequence identity in the ATP binding site of LRRK2, such as ALK,[43,44] B-Raf,[45,46,47,48] ERK2,[38] JAK2,[34,49,50,51] IRAK4,[52] Lck,[53] MLK1,[39,54,55] ROCK1[56,33] or TAK1,[57,58] or analysis of ligand-bound X-ray crystal structures with off-target kinases such as TTK,[34] MST3[35] or Tyk2[59] to rationalize selectivity. Roco4, a LRRK2 homolog from amoeba, has been used to approximate some aspects of the human LRRK2 ATP binding site.[60] More recently, ligand bound crystal structures of selective LRRK2 inhibitors in complex with a humanized form of Roco4 have been described, in which two point mutations give the surrogate increased resemblance to LRRK2.[61] We report herein the design of a LRRK2 surrogate obtained from the introduction of 10 point mutations into checkpoint kinase 1 (CHK1 10-pt. mut.), its validation by comparing the binding affinity of LRRK2 inhibitors with the mutant protein and their LRRK2 G2019S activity, solving X-ray crystal structures of the protein in complex with known literature inhibitors of LRRK2 and comparing these with existing models to rationalize selectivity, and its use in the optimization of a series of arylpyrrolo[2,3-*b*]-pyridine inhibitors.

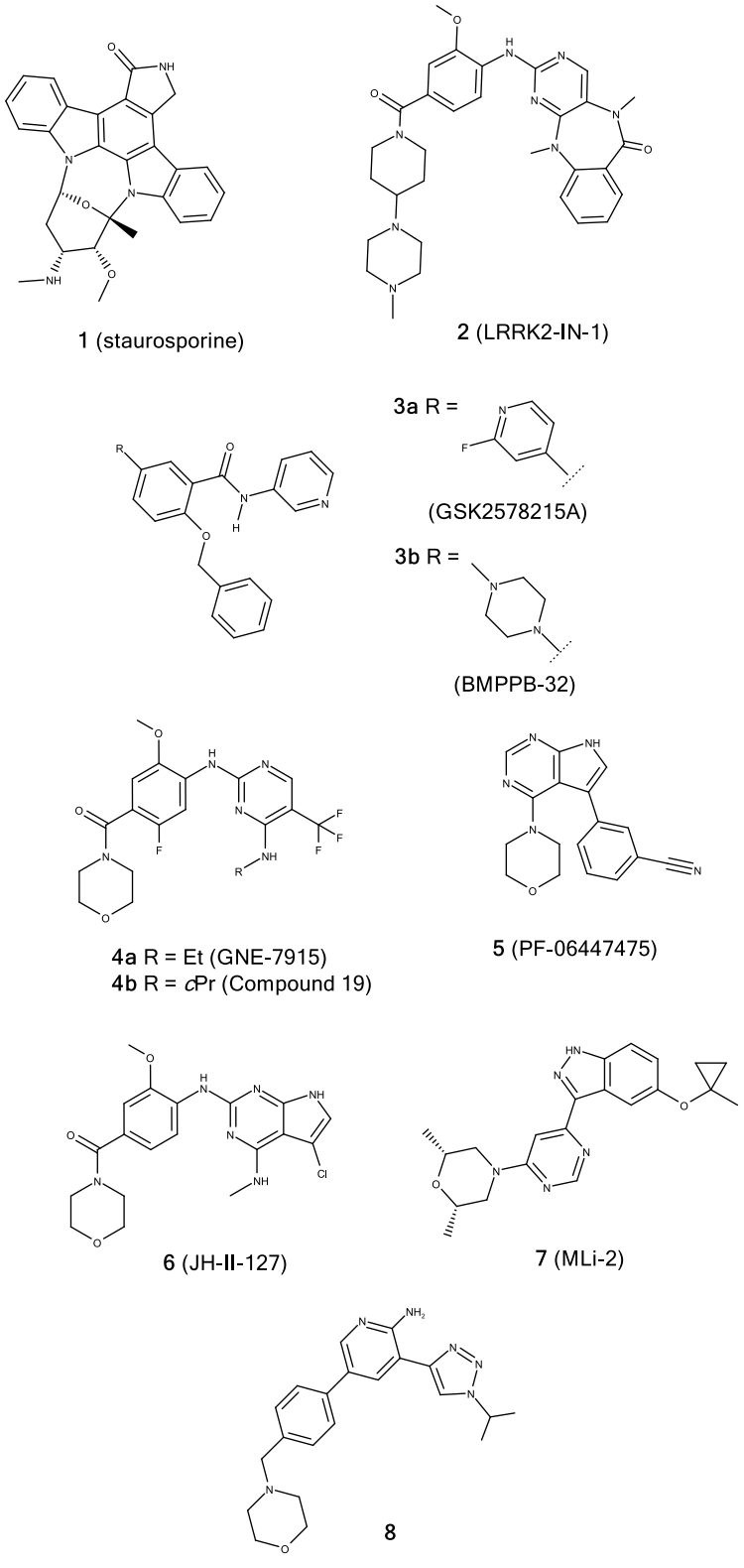

Figure 1. Representative set of reported LRRK2 inhibitors **1**–**8**.

RESULTS AND DISCUSSION

An analysis of the RCSB protein data bank (PDB)[62] identified ten protein kinase structures with >50% ATP binding site similarity to LRRK2. These included mixed-lineage kinase (MLK1), the crystal structure 3DTC[63] of which has formed the basis of LRRK2 homology models previously reported.[39,55,54] CHK1 was selected as a start point, however, guided by previous in-house experience of the expression, purification and crystallization of CHK1 constructs to enable ligand-bound X-ray crystal structures, and their utility in the design of novel inhibitors of this kinase for the treatment of cancer.[64,65] An initial selection of ten residues in CHK1 to be mutated (Figure 2) was based on their <4 Å proximity to **1** in the published ligand bound X-ray structure with CHK1, 1NVR (Figure 3A).[66,67] These residues form key areas of the ATP binding site of the kinase domain, which encompass the hinge, gatekeeper and activation loop. Importantly, the list of mutations also includes areas known for kinase selectivity. Two further constructs, an 8 and 12-pt. mutant of CHK1, were also considered. The latter contained two additional mutations in the flexible glycine-rich loop of the ATP binding site (Ser19 and Phe20, equivalent to Ser1889 and Phe1890 in LRRK2). The 8-pt. mutant was identical to the 10-pt. mutant, but did not bear the F149Y mutation in the activation loop of CHK1 (equivalent to Tyr2018 in LRRK2), nor did it have the G150S mutation (equivalent to the G2019S mutation in LRRK2). Equivalent residues in Roco4[60] and the humanized Roco4,[61] which have been previously reported as LRRK2 surrogates, are also shown in Figure 2.

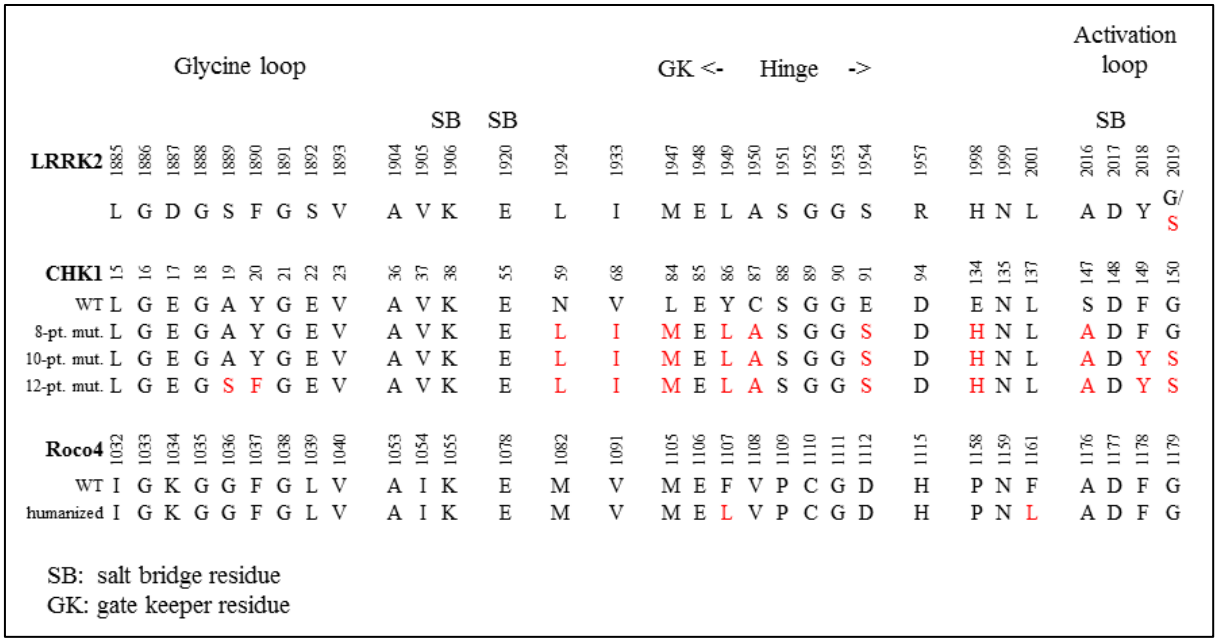

Figure 2. Comparison of selected LRRK2 WT and G2019S mutant ATP binding site residues, with equivalents in CHK1 WT, and 8, 10 and 12-pt. mutants, as well as Roco4 WT[60] and humanized Roco4.[61] Mutations highlighted in red.

The CHK1 10-pt. mut. was investigated as a potential LRRK2 kinase domain surrogate in the first instance, and was successfully expressed in insect cells infected with baculovirus, purified and then crystallized. Following the soak of a protein crystal with **1**, X-ray data were collected and a crystal structure of the resulting protein-ligand complex was obtained (Figure 3B). Reassuringly, binding of the amide moiety of **1** to the hinge via the backbone of Leu86 and Glu85 (equivalent to Leu1949 and Glu1948 in LRRK2, and Tyr86 and Glu85 in CHK1) was similar to that seen in CHK1 structure, 1NVR. A crystal structure of γ-imino-ATP in complex with CHK1 10-pt. mut. was also obtained, and interactions with the ATP binding site were as expected (structure not shown, but deposited in the PDB).

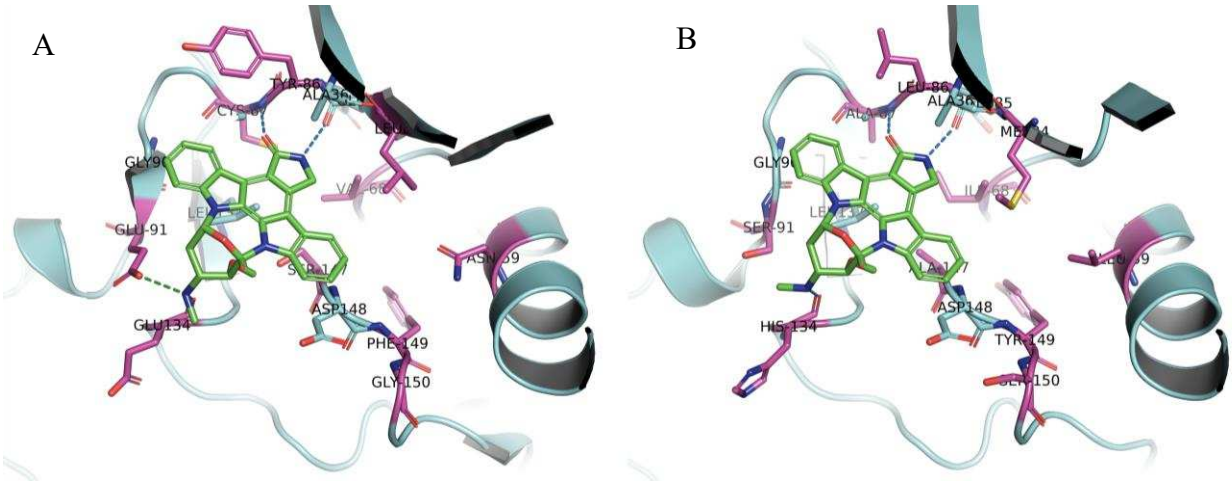

Figure 3(A). X-ray structure of **1** (green)/ CHK1 (cyan) (PDB: 1NVR). (B) X-ray structure of **1** (green)/ CHK1 10-pt. mut. (cyan). Ten residues mutated from CHK1 highlighted in magenta. Key intermolecular contacts are shown as dashed lines (polar ligand to backbone contacts <3.3 Å in blue; polar ligand to sidechain contacts <3.3 Å in green).

With the new LRRK2 kinase domain surrogate in hand, its further usefulness was investigated by soaking selective LRRK2 inhibitors with apo CHK1 10-pt. mut crystals, and obtaining ligand-bound X-ray crystal structures. A structure of **2** with CHK1 10-pt. mut. was obtained (Figure 4A) and compared with the published crystal structure of the same compound in complex with humanized Roco4 kinase (4YZM, Figure 4B).[61] Hydrogen bonds between the backbone carbonyl and NH of Ala87 in the hinge and the aminopyrimidine moiety of **2** are equivalent to those seen between Val1108 and the same ligand in the humanized Roco4 structure. Similarly, the phenyl moiety of the tricyclic core is accommodated by the adenine binding pocket of CHK1 10-pt. mut., and makes contact with Ala147 (equivalent to Ala2016 in LRRK2), which is 3.6 Å away. The other side of the ring is partly covered by the hinge, with the methoxy substituent 3.9 Å away from Leu86 (equivalent to Leu1949 in LRRK2). This interaction is significant for kinase selectivity, since analysis has shown[68] that 40% of kinases have a more sterically encumbered

Tyr and 18% have a Phe in the position equivalent to 1949 (as shown in Figure 3A with CHK1), whereas 25% of kinases have Leu. In both structures, the electron density of the (4-methylpiperazin-1-yl)piperidinyl moiety is weak, since it is solvent exposed and likely very flexible. A difference in the glycine loop placement was observed between the two structures, however. CHK1 10-pt. mut. incorporates Tyr20, whereas humanized Roco4 has Phe1037, identical to Phe1890 in LRRK2. Tyr20 of CHK1 10-pt. mut. makes a polar interaction with the carbonyl group of **2** and Lys38 of the salt bridge (Lys1906 in LRRK2) is more distant. In contrast, the equivalent Lys1055 in the humanized Roco4 structure makes a polar contact with the same carbonyl group of the ligand.

To address the sequence differences in the glycine rich loop, a crystal structure of **2** in complex with a CHK1 12-pt. mutant was also obtained (Figure 4C), in which Ser19 and Phe20 (equivalent to Ser1889 and Phe1890 in LRRK2) were present. The glycine loop also remained in the open position in this structure, and Lys38 (Lys1906 in LRRK2) remained in the same position. It is considered that the flexibility of the glycine loop would enable its adjustment to the bound ligand, regardless of whether residue 20 is Tyr or Phe, and should not be over-interpreted in the structures of complexes with surrogate kinases.

A crystal structure of **2** in complex with a CHK1 8-pt. mutant was also obtained (Figure 4D), identical to the 10-pt. mutant, but without the F149Y and G150S mutations. This was in agreement with the structure obtained with the 10 and 12-point mutants, other than the placement of the flexible (4-methylpiperazin-1-yl)piperidinyl solubilizer. All three structures of the CHK1 mutant complexes with **2** reveal they are good models for LRRK2, as residue 19, 20 and 147 mutations do not play a significant role in the binding of this ligand.

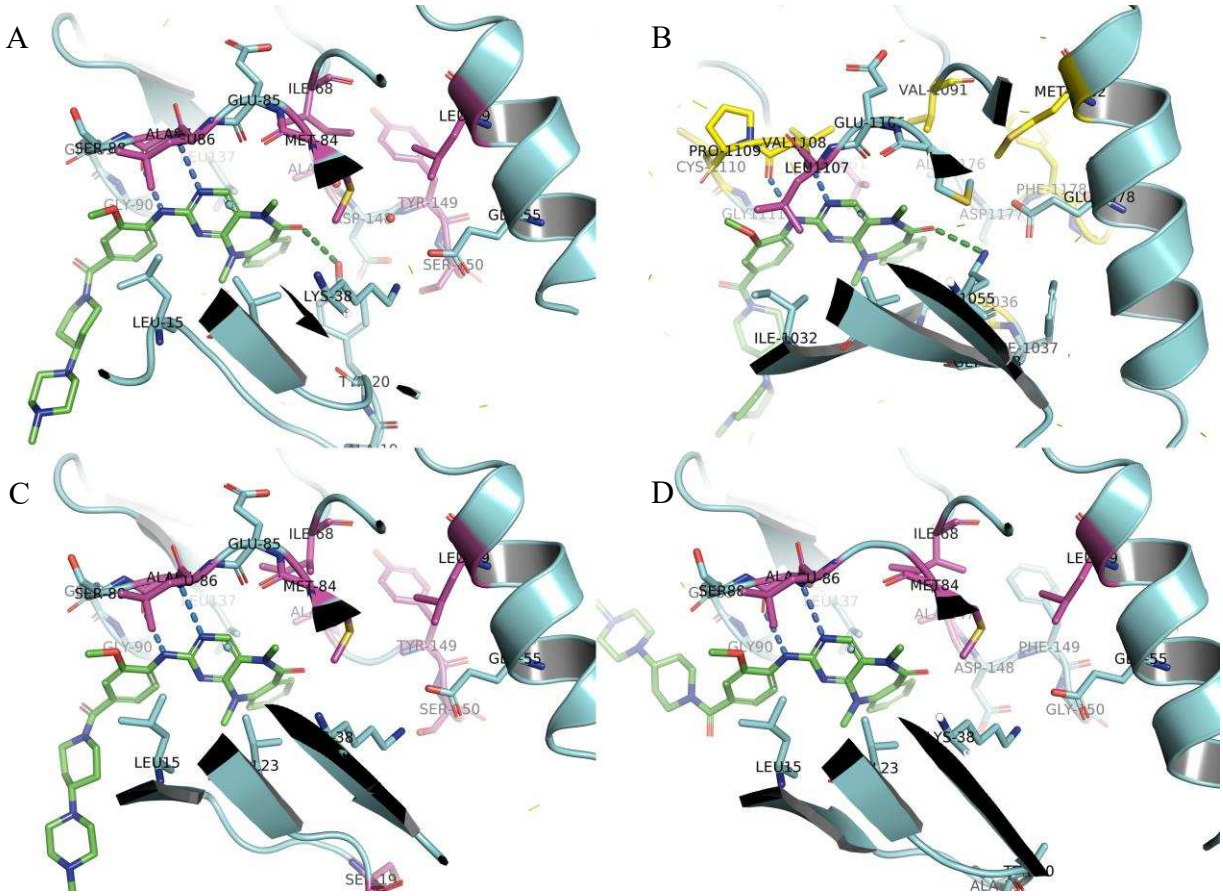

Figure 4. (A) X-ray structure of **2** (green)/ CHK1 10-pt. mut. (cyan). Ten residues mutated from CHK1 highlighted in magenta. (B) X-ray structure of **2** (green)/ humanized Roco4 kinase (cyan).[61] Two residues mutated from Roco4 kinase highlighted in magenta. Residues different to CHK1 12-pt. mut. and LRRK2 G2019S are highlighted in yellow. (C) X-ray structure of **2** (green)/ CHK1 12-pt. mut. (cyan). Twelve residues mutated from CHK1 highlighted in magenta. (D) X-ray structure of **2** (green)/ CHK1 8-pt. mut. (cyan). Eight residues mutated from CHK1 highlighted in magenta. Key intermolecular contacts are shown as dashed lines (polar ligand to backbone contacts <3.3 Å in blue; polar ligand to sidechain contacts <3.3 Å in green).

An X-ray crystal structure of **3a**[33] in complex with CHK1 10-pt. mut. was attempted, to further explore the utility of CHK1 mutants as crystallographic surrogates for LRRK2. Due to the low

solubility of the ligand, and its immediate crystallization in the soaking solution, only partial occupancy of **3a** in the binding site was observed, with the quality of electron density maps and resulting model below accepted standards. Pleasingly, however, a structure of the analogous arylbenzamide **3b**[69,70] in complex with CHK1 10-pt. mut. (Figure 5) was obtained. The ligand adopted a conformation which accommodates an intramolecular hydrogen bond between the arylbenzamide NH and the ether oxygen atom, and is sandwiched between Leu15 of the glycine loop and Leu137, already present in CHK1, and equivalent to Leu1949 and Leu2001 in LRRK2. The crystal structure also showed a polar ligand to backbone interaction between the amide carbonyl of the ligand and mutated Ala87 in the hinge (equivalent to Ala1950 in LRRK2), as well as a hydrophobic contact between the 3-pyridyl moiety of **3b**, Ile68 and gatekeeper Met84 (equivalent to Ile1933 and Met1947 in LRRK2). The *N*-methylpiperazinyl moiety occupies a space next to Leu86 (Ser1951 and Leu1949 in LRRK2), known to impart selectivity for LRRK2 over other kinases with a Phe or Tyr at this position.

The binding mode of **3b** in CHK1 10-pt. mut. is consistent with that reported for **3a** in a LRRK2 homology model based on ROCK1,[33,56] in which the ligand avoids steric clash with Ala2106 in LRRK2 (Ala147 in CHK1 10-pt. mut., 4.2 Å from the pyridyl moiety of the ligand).

Two further X-ray crystal structures of **3b** in complex with the CHK1 8- and 12-pt. mutants were also obtained (not shown, but structures deposited in the PDB), and these structures were highly analogous to that obtained with CHK1 10-pt. mut. Based on the three structures of the CHK1 mutant complexes with **3b**, as well as structures of complexes with **2**, we concluded that the CHK1 10-pt. mut. is a good representation of a LRRK2 kinase domain surrogate, and that protein was then used for all further structure determinations.

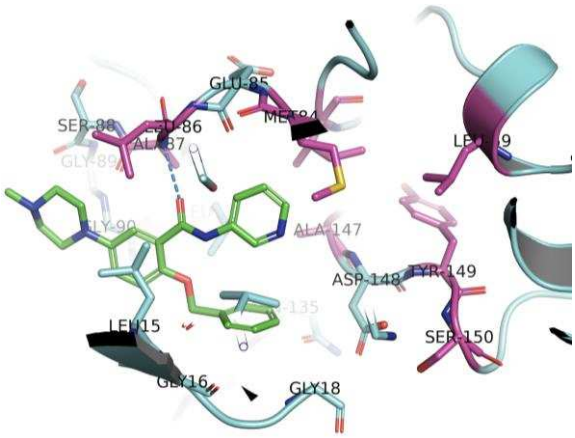

Figure 5. X-ray structure of **3b** (green) in complex with CHK1 10-pt. mut. (cyan). Residues mutated from CHK1 highlighted in magenta. Key polar contacts <3.3 Å in blue dashed lines.

A crystal structure of **4a** in complex with CHK1 10-pt. mut. was also obtained (Figure 6a), and compared with the published structure of analogous **4b**[34] bound to humanized Roco4 (Figure 6b).[61] The hinge binding aminopyrimidine moiety of **4a** forms characteristic hydrogen bonds with the backbone carbonyl and NH of Ala87 in CHK1 10-pt. mut. (Ala1950 in LRRK2), which are equivalent to those seen between **4b** and Val1108 in the humanized Roco4 structure. The trifluoromethyl substituent of **4a** forms multiple hydrophobic contacts with Val23 of the glycine loop, Ile68, Met84 gatekeeper, Leu137 and Ala147 of the activation loop, which are comparable with interactions between the same moiety of **4b** and Val1040, Val1091, Met1105, Leu1161 and Ala1176 in the humanized Roco4 structure. The trifluoromethyl group of **4a** makes a water mediated contact with Glu55 (Glu1920 in LRRK2) of the α-helix, in a similar fashion to that of **4b** and Glu1078 of Roco4. A water mediated contact between the ligand and Asp148 (Asp2017 in LRRK2) of the activation loop is not observed, as is seen with the equivalent Asp1177 in the Roco4 structure, since Asp148 makes a hydrogen bond contact with Ser150, equivalent to Ser2019 in the LRRK2 G2019S mutant. Additionally, a water mediated contact is observed between the fluoro substituent of **4a** and Ser91 in the hinge (equivalent to Ser1954 in LRRK2).

This residue remains as Asp1112 in the Roco4 structure. The methoxy group of **4a** occupies space in the roof of the hinge created by the backbone of Ser88 and residue of Leu86, equivalent to Pro1109 (which confers additional rigidity on the protein backbone in comparison with LRRK2) and Leu1107 in the Roco4 structure. The morpholino moiety of **4a** has some electron density; this part is solvent exposed, and not recognized specifically by the kinase domain.

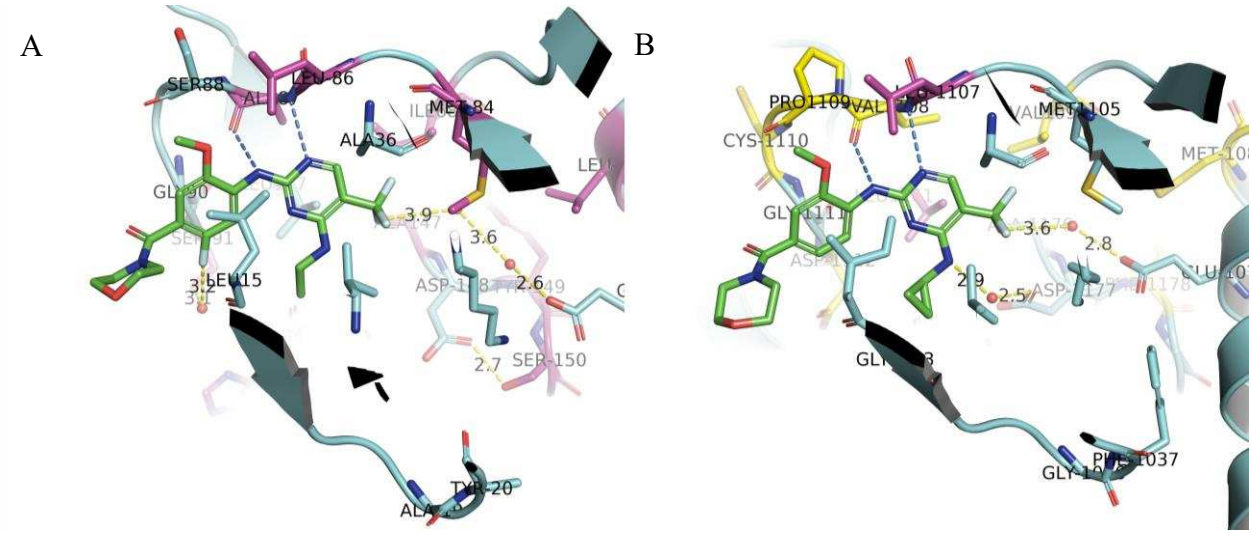

Figure 6. X-ray structure of (A) **4a** (green) in complex with CHK1 10-pt. mut. (cyan), and (B) **4b** (green) in complex with humanized Roco4 kinase (cyan).[61] Mutated residues are highlighted in magenta. Residues different to CHK1 10-pt. mut. and LRRK2 G2019S in humanized Roco4 are highlighted in yellow. Polar intermolecular contacts <3.3 Å are shown as dashed lines.

Similar relationships between LRRK2 selectivity and binding mode in the surrogate were observed in other inhibitor chemotypes disclosed more recently. Indazole **7** bears a 1-methylcyclopropoxy substituent, the methyl group of which is placed 4 Å from Ala147 in the CHK1 10-pt. mut. crystal structure (Ala1950 in LRRK2), whilst the cyclopropyl moiety is enclosed by the glycine-rich loop, including hydrophobic interaction with Val23 (Val1893). The 2,6-dimethylmorpholinyl moiety occupies the space next to Leu86, analogous to Leu1949 in

LRRK2. These interactions are in agreement with those observed un an ERK2-dervived homology model.[38] Aminopyridine **8**[39] adopts a conformation in which one methyl group of its isopropyl substituent is 4.2 Å away from Ala147 and C6 of the pyridine ring sits 3.7 Å from Leu86; it is likely that both hydrophobic contacts increase selectivity for LRRK2.

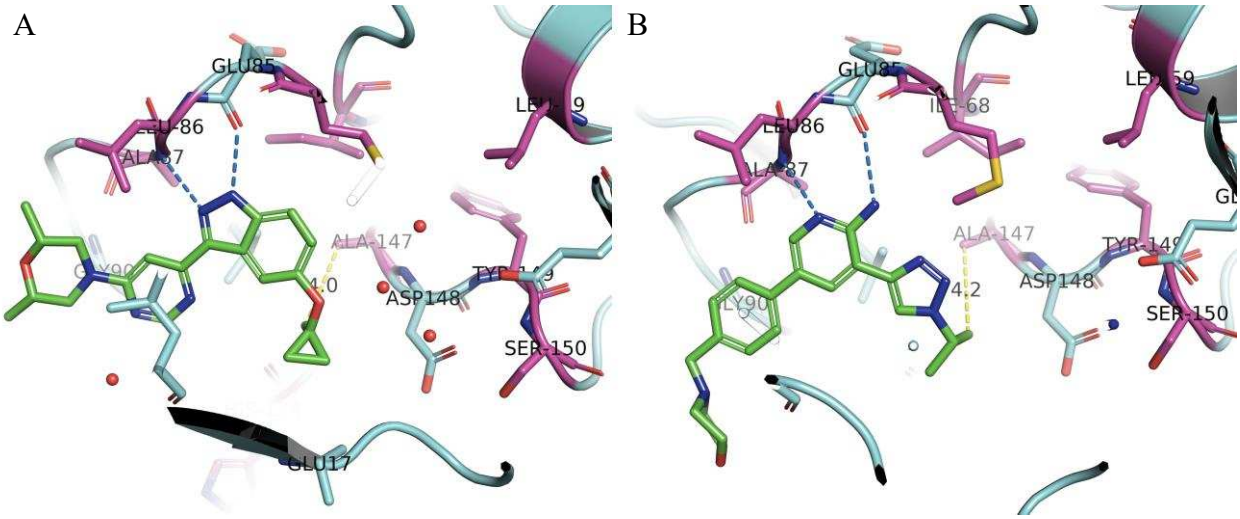

Figure 7. X-ray structures of (A) indazole **7** and (B) 2-aminopyridine **8** (green) in complex with CHK1 10-pt. mut. (cyan). Mutated residues are highlighted in magenta. Polar intermolecular contacts <3.3 Å are shown as dashed lines.

The LRRK2 G2019S activity of 41 LRRK2 inhibitors previously described in the literature, including 2-aminopyridines,[39] and also pyrrolopyridines disclosed herein was determined, and compared with binding affinity for CHK1 10-pt. mut. in a LanthaScreen europium binding assay (Figure 8). Correlation coefficient (r^2) was 0.57 and Spearman's rho rank correlation coefficient was 0.77, showing a reasonable statistical dependence between the two variables. In contrast, there was no correlation between LRRK2 G2019S activity and CHK1 binding affinity (see supporting information), thus providing further evidence for the utility of the CHK1 10-pt. mutant as a LRRK2 surrogate.

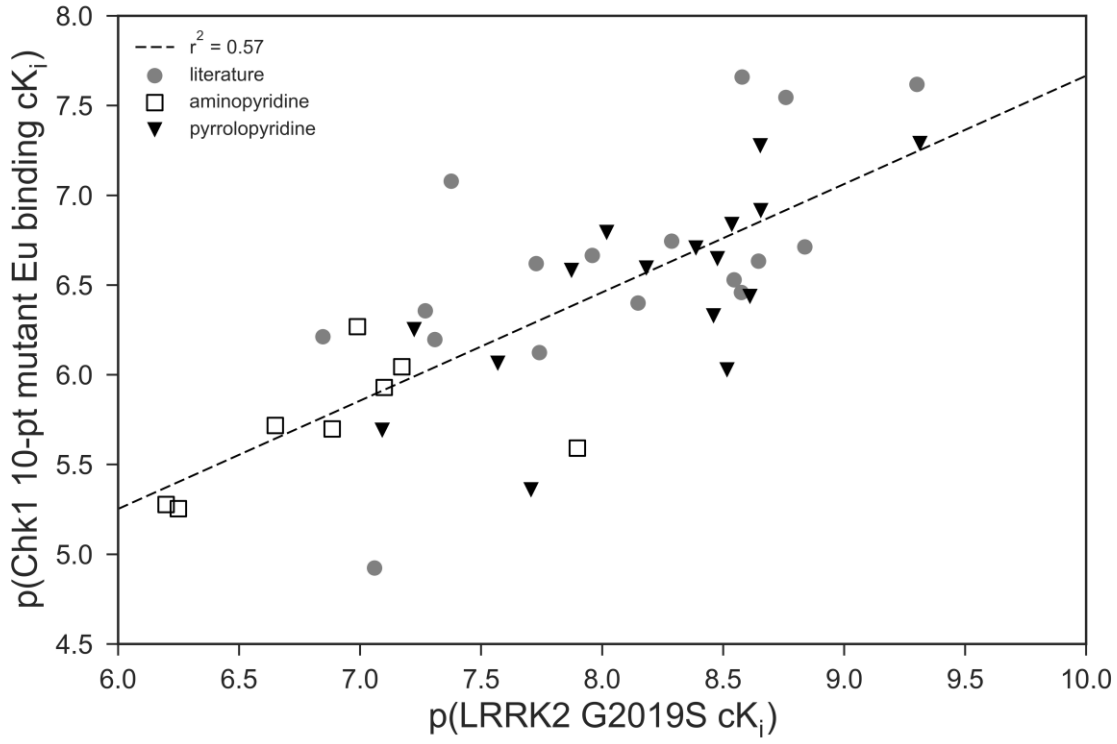

Figure 8. Plot of *p*(LRRK2 G2019S Lanthascreen activity cK_i) vs *p*(CHK1 10-pt mut. binding affinity cK_i) for 41 LRRK2 inhibitors.

Pyrrolopyrimidines[35,36,71] and pyrrolopyridines[72] have been under investigation as LRRK2 inhibitors by a number of groups. A crystal structure of highly potent and brain penetrant **5** in complex with CHK1 10-pt. mut. was obtained (Figure 9A). Binding of the ligand to the hinge via the backbone of Ala87 and Glu85 (equivalent to Ala1950 and Glu1948 in LRRK2) was observed, and the bicyclic core is positioned 3.6 Å from Leu86 (Leu1949 in LRRK2) in the roof of the hinge. The nitrile group makes a weak hydrogen bond to Lys38 (3.7 Å), and a water mediated contact with Glu55 of the α-helix. These data are in good overall agreement with the published structure of **5** in complex with MST3 (PDB code 4U8Z),[35] however MST3 does not

bear the Y101L mutation, equivalent to Leu86 in CHK1 10-pt. mut, and Leu1949 in LRRK2, which may enable binding of more selective ligands.

A crystal structure of CHK1 10-pt. mut. and **6**, reported as high potent, selective and brain penetrant LRRK2 inhibitor,[36] was also obtained (Figure 9B). Key ligand-protein interactions were in line with a reported docking study based on Roco4 kinase, which predicted three hydrogen bonds from the pyrrolopyrimidine to the hinge via Leu1949 and Ala1950. Additionally, docking suggested the possibility of a halogen interaction with the gatekeeper Met1947 and the 5-chloro substituent of the ligand. The equivalent interactions with Leu86, Ala87 and Met84 in CHK1 10-pt. mut. were observed. In addition, the 5-chloro substituent makes a water mediated interaction with the salt bridge comprised of Lys38 and Asp148, as well as Glu55. The methoxy group sits between the Leu86 residue and Ser88 backbone in the hinge extension, and the amide carbonyl sits out-of-plane, making a water-mediated contact with Asp94, so that the morpholine substituent tucks under the glycine loop. Asp94 is equivalent to Arg1957 in LRRK2, His1115 in Roco4 and Asp109 in MST3; there is therefore potential in LRRK2 for a direct contact between Arg1957 and the amide carbonyl, which is not observed in these surrogates.

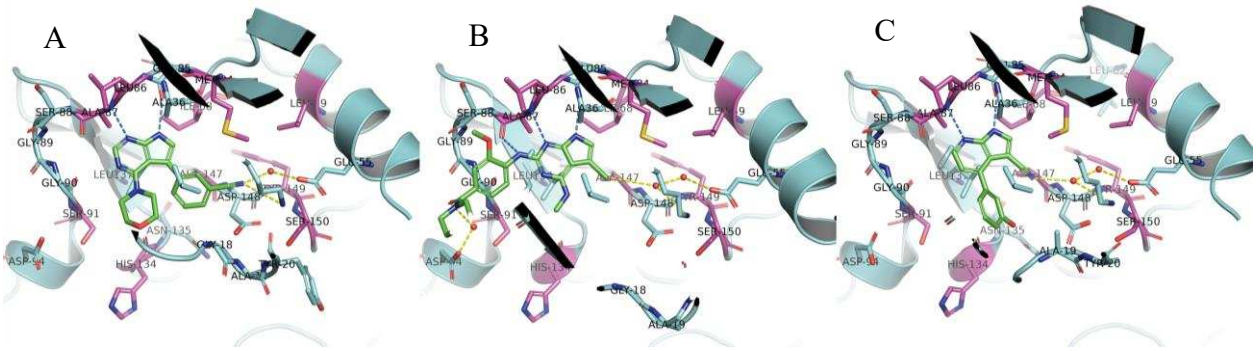

Figure 9. X-ray crystal structures of pyrrolopyrimidines (A) **5** and (B) **6**, and (C) pyrrolopyridine **9** (green) in complex with CHK1 10-pt. mut. (cyan). Residues mutated from CHK1 highlighted

in magenta. Key polar contacts <3.3 Å indicated with blue dashed lines. Likely water-mediated hydrogen bonds indicated in yellow dashed lines.

The present authors identified pyrrolopyridine **9**[73] [LRRK2 G2019S IC_{50} 415 nM, cK_i 27 nM,[74] ligand efficiency (LE)[75] 0.58] in a biochemical screen of an in-house library focused on low molecular weight compounds with known kinase hinge binding motifs (Table 1). This was a representative of fragment hit 1*H*-pyrrolo[2,3-*b*]pyridine (48% @ 200 μM, estimated K_i 15 μM, LE 0.74) which arose from a fragment library screen which was also conducted using the same biochemical assay format. An X-ray crystal structure of **9** in complex with CHK1 10-pt. mut. was obtained (Figure 9C). Binding of **9** to the hinge via the backbone of Ala87 and Glu85 (equivalent to Ala1950 and Glu1948 in LRRK2) was observed, and the bicyclic core is positioned 3.9 Å from Leu86 (Leu1949 in LRRK2) in the roof of the hinge. The nitrile moiety sits close to the Met84 gatekeeper (Met1947 in LRRK2), and picks up water mediated interactions with the salt bridge comprised of Asp148 and Lys38, as well as a water mediated contact with Glu55 of the α-helix. Subsequent screening of fragments **10**[76,73] (cK_i ~3 μM, LE 0.68) and **11**[73] (cK_i ~2 μM, LE 0.65) indicated that a significant binding efficiency arose from the polar interactions in the hinge and water mediated contact with the salt bridge via the nitrile.

The phenol substituent of **9**, positioned between the flexible Gly loop, Ala147 and Asp148, underwent initial optimization. The corresponding phenyl and thiophen-3-yl analogues **12** and **13**[76] had activities within three-fold of the start point **9**. Chloro or methyl substitution of the phenyl ring of **9** (**14**–**19**) indicated that the *meta*-substituted examples **15** and **18** were better tolerated than *ortho* or *para*. This was further confirmed by 3-methoxy derivative **20** (cK_i 24 nM). 6-Amino substitution of the pyrrolopyridine core of **12** was carried out, with a view to enhancing interaction with the hinge region of the ATP binding site of the kinase. This gave rise

to **21** (cK_i 12 nM), which was seven-fold more potent on LRRK2. A similar uplift in potency was observed with the 6-amino derivative of **18**; **22** had a LRRK2 G2019S cK_i of 2 nM, whilst maintaining a high LE of 0.62. LRRK2 WT activities of compounds were in agreement with those determined on LRRK2 G2019S, and these data are also presented in Table 1.

Table 1. LRRK2 G2019S and WT Lanthascreen activity of pyrrolo[2,3-*b*]pyridines **9**–**22**.

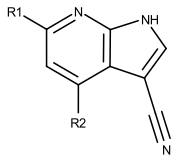

			LRRK2 Lanthascreen activity					
			G2019S			WT		
Compd	**R^1**	**R^2**	**IC_{50} (nM)[a]**	**cK_i (nM)**	**LE**	**IC_{50} (nM)[b]**	**cK_i (nM)**	**LE**
9	H	3-Hydroxyphenyl	415	27	0.58	487	13	0.60
10	"	H	46522	2702	0.68	101080	3026	0.66
11	"	Cl	37765	2193	0.65	n.d.		
12	"	Phenyl	1178	81	0.57	954	23	0.62
13	"	Thiophen-3-yl	870	60	0.61	1279	31	0.65
14	"	2-Chlorophenyl	9271	538	0.47	7531	225	0.49
15	"	3-Chlorophenyl	1275	81	0.54	784	23	0.59
16	"	4-Chlorophenyl	1983	136	0.50	n.d.		
17	"	2-Methylphenyl	27838	1617	0.44	26163	783	0.47

18	"	3-Methylphenyl	195	13	0.60	170	4	0.64
19	"	4-Methylphenyl	1639	95	0.54	4135	124	0.53
20	"	3-Methoxyphenyl	354	24	0.55	247	6	0.59
21	NH_2	Phenyl	176	12	0.61	140	3	0.65
22	"	3-Methylphenyl	33	2	0.62	21	0.5	0.67

[a]250 pM protein, 1.3 mM ATP. [b]1 nM protein, 1.3 mM ATP; n.d., not determined.

An X-ray crystal structure of **22** in complex with CHK1 10-pt. mut. was obtained (Figure 10A). As also seen with the original hit **9**, binding of the ligand to the hinge via the backbone of Ala87 and Glu85 (equivalent to Ala1950 and Glu1948 in LRRK2) was observed. The nitrile group is also placed next to the Met84 gatekeeper, and links via waters to the salt bridge comprised of Lys38, Glu55 and Asp148. The 3-tolyl substituent is bounded by the Gly loop, with which it likely makes van der Waals interactions. The methyl group points towards a small hydrophobic pocket formed of Ala147 and the stem of Asp148. Ala147, equivalent to Ala2016 in LRRK2, is not well conserved across the kinome, and interaction in this region of space likely imparts selectivity for LRRK2.

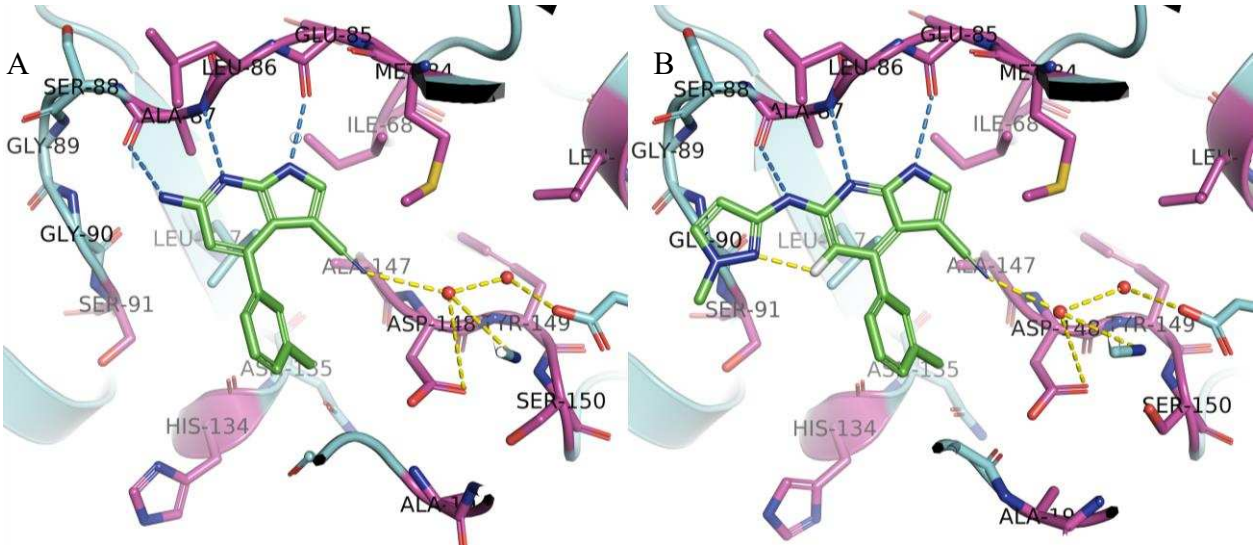

Figure 10. X-ray crystal structures of (A) **22** and (B) **23** (green) in complex with CHK1 10-pt. mut. (cyan). Residues mutated from CHK1 highlighted in magenta. Key polar contacts <3.3 Å indicated with blue dashed lines. Likely intramolecular and water-mediated hydrogen bonds indicated in yellow dashed lines.

Phosphorylation sites, including Ser935 and Ser1292, have been used as pharmacodynamic markers for LRRK2 target engagement *in vitro* and in *vivo*.[77] Further evidence for the interaction

of **22** with Ala2016 was therefore obtained from in-cell western (ICW) assay-based LRRK2 IC_{50} values, which were determined using HEK293 LRRK2-pSer935 assays in either a 96-well (transient transfected cells) or a 384-well set-up (BacMam transduced cells). **22** had LRRK2-pSer935 IC_{50} values of 24 nM, 40 nM and 471 nM for LRRK2 WT, G2019S and A2016T, respectively (Figure 11 and Table 2, 96-well assay). In a 384-well set-up, **22** showed similar potencies in ICW LRRK2 G2019S cell-based Ser935 and Ser1292 phosphorylation assays, with IC_{50} values of 70 nM and 61 nM, respectively (Table 2).

The ~10-fold drop in potency of **22** between LRRK2 WT and G2019S when compared to A2016T that is observed in the cell-based assay is in agreement with the crystallographic evidence obtained from the CHK1 10-pt mut. that **22**, via the methyl group on the tolyl substituent, engages with Ala2016 in both human LRRK2 WT and G2019S.

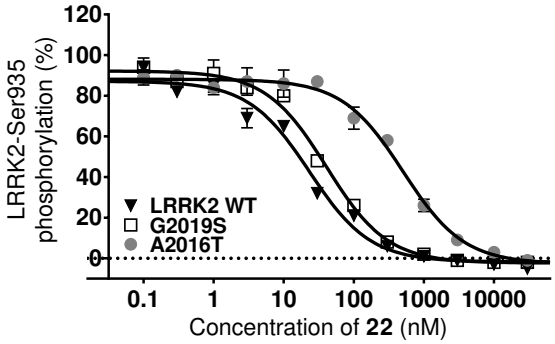

Figure 11. ICW assay data showing inhibition of LRRK2-Ser935 phosphorylation in HEK293 cells overexpressing LRRK2 WT, and the G2019S and A2016T mutants, by **22**.

Table 2. Cell-based IC_{50} values of **22** on LRRK2 WT, G2019S and A2016T.

LRRK2 variant	LRRK2-pSer935 (96-well)[a]		LRRK2-pSer935 (384-well)[b]		LRRK2-pSer1292 (384-well)[b]	
	IC_{50} (nM)	pIC_{50}	IC_{50} (nM)	pIC_{50}	IC_{50} (nM)	pIC_{50}
WT	24	7.61±0.06 (n = 3)	67	7.17±0.20 (n = 6)	n.d.	
G2019S	40	7.40±0.01 (n = 3)	70	7.16±0.16 (n = 6)	61	7.21±0.17 (n = 3)
A2016T	471	6.33±0.05 (n = 3)	n.d.		n.d.	

[a]Transient transfection LI-COR ICW assay (HEK293).[70]

[b]BacMAM LI-COR ICW assay (HEK293); n.d., not determined.

22 had moderate MDCK-MDR1 permeability (P_{app} A:B 8.6 cm/sec x 10^{-6}), low efflux ratio (B:A/A:B 0.7) and moderate rat and human microsomal clearance (9 and 1.5 L/kg/h, respectively). Pharmacokinetic and pharmacodynamic profiling on **22** in wild-type mice was performed using LRRK2 phosphorylation at serine 935 as the readout for LRRK2 inhibition (Figure 12). Following 25 mg/kg oral dosing of **22** in wild-type mice, full LRRK2 inhibition in mouse brain was observed for at least 12 h. The mean unbound drug concentration at 12 h was 10 ng/g (~40 nM). LRRK2-pSer935 levels were back to 80% 24 h after dosing.

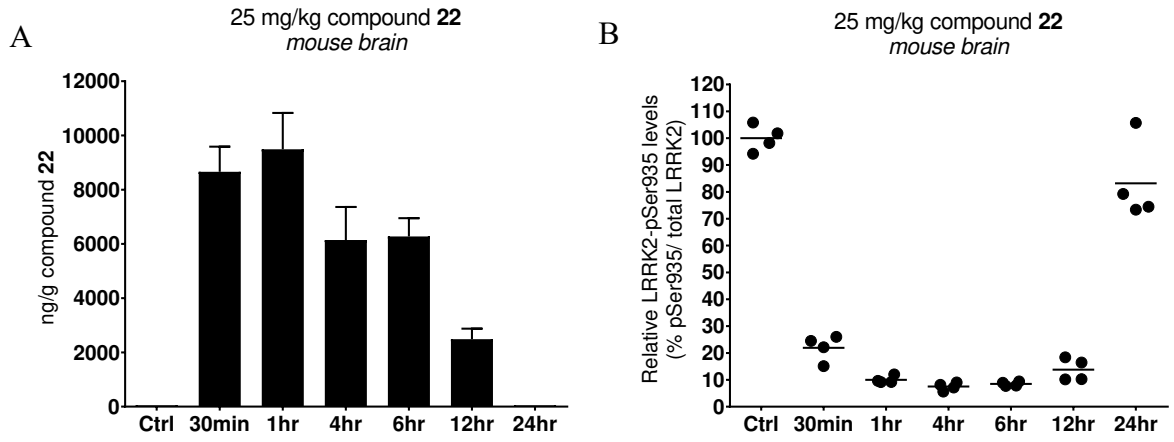

Figure 12. Pharmacokinetic and pharmacodynamic profile of **22** in mouse brain following 25 mg/ kg po dosing: (A) exposure of **22** over 24 hours, (B) relative LRRK2-pSer935 levels in mouse brain over 24 hours.

Further *in vivo* exploration at C_{max} in wild-type mice found that LRRK2-pSer935 IC_{50} values for **22** in mouse brain and kidney were 1.3 nM and 5 nM, respectively (Figure 13A and B).

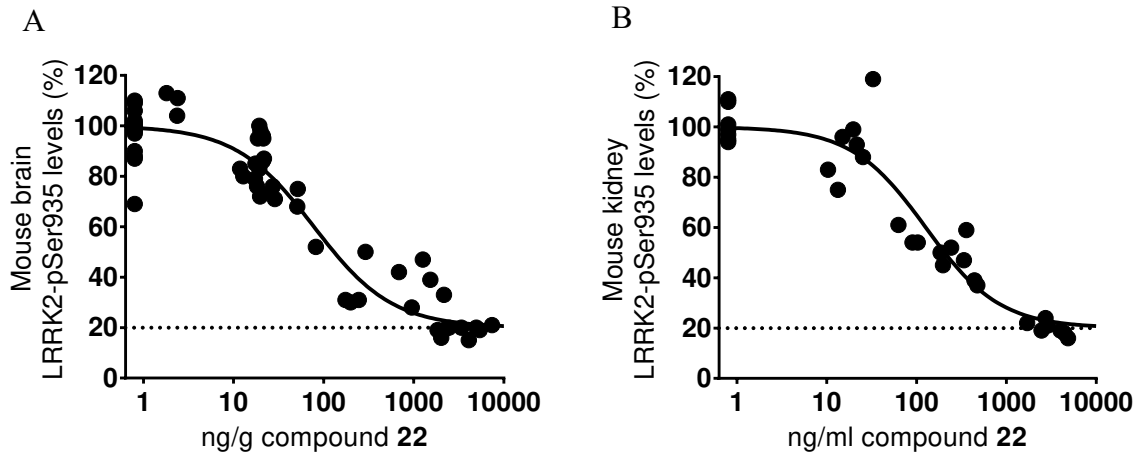

Figure 13. Dose-response relationship of **22** in mouse brain and kidney: (A) brain studies (n=3), (B) mouse kidney studies (n=2). LRRK2-pSer935 levels were assessed one hour after po dosing; the data were used to estimate IC_{50} values for **22**.

Assessment of the *in vitro* kinase selectivity of **22** by a DiscoveRx KINOMEscan assay at 1 μM identified 21 off-target hits with % control <5% (i.e. >95% inhibition), including JAK3, Tyk2 and TTK, indicating that further improvement to selectivity would be required. **22** was also assessed in cultured human peripheral blood mononuclear cells (PBMCs) using ActivX KiNativ technology,[78] in order to give further indication of LRRK2 potency and a wider assessment of kinase selectivity. **22** gave 91% inhibition on LRRK2 @ 1 μM, with no inhibition of other kinases >60% (including JAK3; Tyk2 and TTK were not present in this panel). **22** also underwent broad *in vitro* pharmacology profiling by Eurofins CEREP at 1 μM. Although **22** showed radioligand binding affinity for adenosine A_1, A_{2A}, A_3 and 5-HT_{2B} receptors, no significant agonist or antagonist effects were observed at doses up to 10 μM in follow-up studies. **22**, however, gave positive results in an Ames bacterial mutagenicity assay and also during assessment of compound-induced genomic instability in TK6 cells. Further optimization, with a focus on improving potency and kinase selectivity, was therefore required.

1-Methyl-1*H*-pyrazol-3-yl substitution on the primary amino group of **22** gave rise to **23**[76] which had increased LRRK2 G2019S IC_{50} 8 nM (cK_i 0.1 nM) (Table 3). An X-ray crystal structure of **23** in complex with CHK1 10-pt. mut. was obtained (Figure 10B), in which the ligand forms the same interactions as **22**. In addition, **23** adopts a conformation such that the 6-(1-methyl-1*H*-pyrazol-3-yl)amino substituent forms an intramolecular hydrogen bond between N2 of the pyrazole and the CH of the pyrrolopyridine core. C4 and 5 of the pyrazole ring also makes van der Waals contact with Gly90 in the roof of the hinge (Gly1953 in LRRK2), which likely explains the increased potency on LRRK2.

23 also had enhanced activity in the LRRK2 G2019S-pSer935 HEK293 ICW 384-well assay, with IC_{50} 18 nM. The aqueous solubility of crystalline material was low (<0.1 μg/ ml), however

MDCK-MDR1 permeability was moderate (P_{app} A:B 8.8 cm/sec x 10^{-6}), and efflux ratio was low (B:A/A:B 0.6). Rat and human microsomal clearance were 6 and 8.5 L/kg/h respectively, indicating a disconnect between the two species. Following 10 mg/ kg po dosing of **23** in mouse, there was no plasma exposure. A vehicle screen, followed by sc dosing in mouse of 2 mg/kg resulted in a maximum brain concentration of 25 ng/g, at time points of 30 min and 1 hour after dosing. The free brain concentration was ≈ 0.025 ng/g (corresponding to 0.076 nM, close to the LRRK2 G2019S cK_i of 0.1 nM). **23** was also assessed in human cultured PBMCs using the ActivX KiNativ assay. Encouragingly, **23** gave 83% inhibition @ 100 nM on LRRK2 and 93% inhibition @ 1 μM. At 100 nM, there was no inhibition of other kinases, and at 1 μM, there was no inhibition of other kinases >50%, other than JAK1 (55%), JAK3 (53%) and JNK1 (71%).

Modifications to the structure of **23** were carried out, with a view to optimizing its physicochemical properties, and thus PK profile, for exposure in the CNS (Table 3). Removal of the methyl substituent (**24**) reduced human microsomal clearance significantly. This also led to a reduction in LRRK2 activity of **24**, however, likely explained by loss of hydrophobic contact between the methyl group and stem of Asp148 and Ala147 in CHK1 10-pt. mut. Replacing R^2 with a range of methylpyridyl substituents was also explored (**25–28**). This led to a reduction in human microsomal clearance in each case; however, the 4-methylpyridin-2yl analogue **25** was significantly less active in the LRRK2 kinase assay. It is likely that introduction of a nitrogen atom at this position would encourage co-planarity between the bicyclic core of the molecule and the pyridyl substituent, thus disrupting hydrophobic contacts with the molecule. Additionally, the nitrogen atom would likely be positioned in the vicinity of the conserved Val23 residue of the Gly loop, with which it would form an unfavorable interaction. Furthermore, **25–28** had an efflux ratio of >2, and therefore unlikely to have the desired CNS exposure *in vivo*.

4-Substitution on the pyrazole ring was well tolerated in the LRRK2 enzyme and cell assays (**29**–**31**), which is consistent with space being available in the hinge extension adjacent to Leu86, as shown in the crystal structure of **23** (Figure 10B). Unfortunately, this modification led to increased microsomal clearance and efflux. 4-Chloro substitution on the pyrazole ring was also well tolerated in the LRRK2 enzyme and cell assays. In comparison with methyl derivatives **29**–**31**, **32**–**34** had lower efflux ratio. This was still in excess of 2, however, and high human microsomal clearance rendered compounds from this series unsuitable for further progression.

Table 3. LRRK2 G2019S and WT Lanthascreen and cell-based activity, human liver microsomal clearance, MDR1-MDCK permeability and efflux ratio of pyrrolo[2,3-*b*]pyridines **23**–**34**.

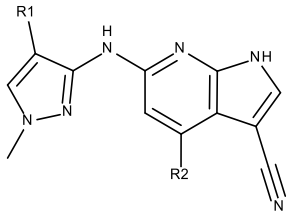

Compd	R^1	R^2	LRRK2 kinase activity		LRRK2 pSer935 HEK293 (384-well)		HLM CL (mL/min /Kg)	P_{app} A:B (MDCK) (cm/sec × 10^{-6})	B:A/ A:B
			G2019S IC_{50} (nM)[a]	WT IC_{50} (nM)[b]	G2019S IC_{50} (nM)[c]	WT IC_{50} (nM)			
23	H	3-Methylphenyl	8	3	18	17	8.5	8.8	0.6
24	"	Phenyl	112	99	100	85	4.5	5.9	0.4
25	"	4-Methylpyridin-2-yl	324	205	n.d.	n.d.	1.3	5.0	4.2
26	"	5-Methylpyridin-3-yl	37	27	90	70	2.3	2.3	3.6
27	"	2-Methylpyridin-4-yl	55	102	130	700	2.9	2.5	2.3
28	"	6-Methylpyridin-2-yl	41	28	160	76	1.0	5.2	4.9
29	Me	5-Methylpyridin-3-yl	48	43	170	160	3.8	0.9	17.5
30	"	2-Methylpyridin-4-yl	108	215	210	580	4.7	1.7	17.0

31	"	6-Methylpyridin-2-yl	50	36	170	130	2.1	1.6	27.7
32	Cl	5-Methylpyridin-3-yl	68	67	190	93	4.2	3.6	4.2
33	"	2-Methylpyridin-4-yl	158	180	210	1300	4.8	4.1	4.5
34	"	6-Methylpyridin-2-yl	57	44	94	110	2.8	2.8	7.9

[a]250 pm protein, 1.3 mM ATP. [b]1 nM protein, 1.3 mM ATP. [c]n.d., not determined.

CHEMISTRY

The synthesis of **12**–**21** is summarized in Scheme 1. Commercially available **11** underwent Suzuki cross-coupling with boronic acids to give **12**–**20** directly. Treatment of **11** with *m*-CPBA, followed by methansesulfonic acid, afforded the *N*-oxide **35**. Subsequent treatment of **35** with dimethyl sulfate and then 7N ammonia in methanol afforded **36**, which underwent Suzuki cross-coupling with phenylboronic acids to give **21**.

Scheme 1. Synthesis of compounds **12**–**21**.[a]

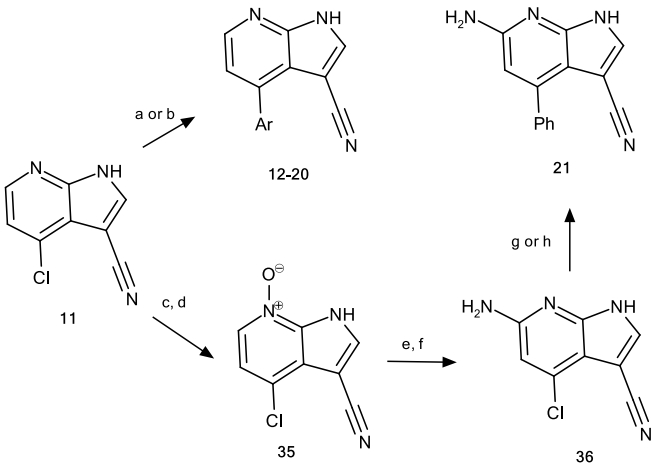

[a]Reagents and conditions: (a) $ArB(OH)_2$, KF, $[(tert\text{-}Bu)_3P]_2Pd(0)$, 1,4-dioxane, H_2O, 150 °C; (b) $ArB(OH)_2$, K_2CO_3, $Pd(dppf)Cl_2$, THF, H_2O, 120 °C; (c) *m*-CPBA, $CHCl_3$, 0° C to rt; (d) $MeSO_3H$; (e) Me_2SO_4, MeCN, 60 °C; (f) 7N NH_3/ MeOH, 70 °C; (g) $ArB(OH)_2$, KF, $[(tert\text{-}Bu)_3P]_2Pd(0)$, 1,4-dioxane, H_2O, 120 °C; (h) $PhB(OH)_2$, K_2CO_3, $Pd(dtbpf)Cl_2$, THF, H_2O, 120 °C.

The synthesis of **22** is summarized in Scheme 2. Trimethylsilylethoxymethyl (SEM) protection of **11** gave **37**, which underwent Suzuki coupling to give **38**; subsequent SEM deprotection with TBAF gave **18**. Treatment of **18** with *m*-CPBA, followed by methansesulfonic acid, afforded the *N*-oxide **39**. Reaction of **39** with methanesulfonyl chloride gave intermediate **40**, which underwent reaction with LHMDS followed by XPhos and tris(dibenzylideneacetone)dipalladium(0) to give **22**.

Scheme 2. Synthesis of compound **22**.[a]

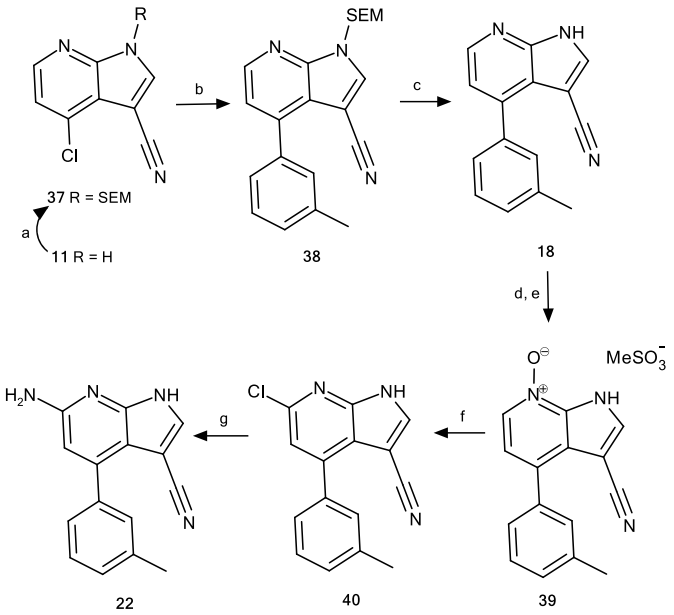

[a]Reagents and conditions: (a) SEMCl, NaH, DMF, 0 °C to rt; (b) 3-MePhB$(OH)_2$, Cs_2CO_3, $Pd(PPh_3)_4$, 1,4-dioxane, H_2O, 100 °C; (c) TBAF, Et_3N, THF, 70 °C; (d) *m*-CPBA, CH_2Cl_2, 0° C to rt; (e) $MeSO_3H$, rt; (f) $MeSO_2Cl$, DMF, 80 °C; (g) LiHMDS, XPhos, $Pd_2(dba)_3$, THF, 60 °C.

The synthesis of **23**–**34** is described in Scheme 3. Reaction of *N*-oxide intermediate **35** with methanesulfonyl chloride gave 4,6-dichloro-1*H*-pyrrolo[2,3-*b*]pyridine-3-carbonitrile **41**. Buchwald-Hartwig amination of **41** with 1-Me-1*H*-pyrazol-3-amine gave **42** (R^1 = H), which underwent Suzuki cross-coupling with boronic acids to give **23** or **24** (Method A). The remaining analogues **25**–**34** were prepared by conversion of **41** to the 6-chloro-4-iodo-derivative **43**. Where R^2 = 5-methylpyridin2-yl, **43** underwent Suzuki coupling with a boronic acid and the resulting product **44** underwent treatment with SEM chloride to give **45a** (Method B). For analogues where R^2= 4- or 6-methylpyridin-2-yl, SEM protection of intermediate **43** gave **46**, which underwent Stille coupling with pyridinyl stannanes to afford **45b** or **45c** (Method C). Where R^2 = 2-methylpyridin-4-yl, Suzuki coupling of **46** with a boronic acid gave **45d** (Method D). Intermediates **45a–d** underwent Buchwald-Hartwig amination with a range of 4-substituted 1-Me-1*H*-pyrazol-3-amines to give intermediates of type **47a–j**, which underwent deprotection to give **25**–**34**.

Scheme 3. Synthesis of compounds **23**–**34**.[a]

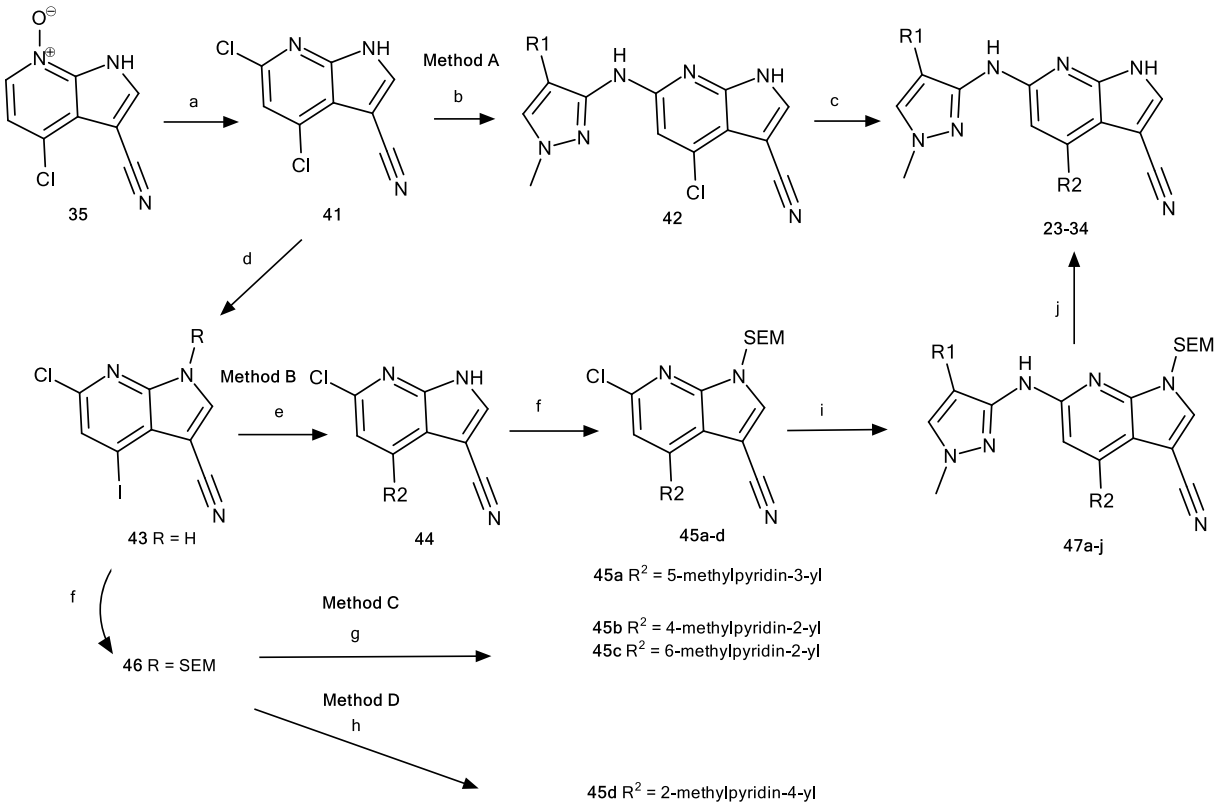

[a]Reagents and conditions: (a) $MeSO_2Cl$, DMF, 80 °C; (b) 1-Me-1*H*-pyrazol-3-amine, (*tert*-Bu)ONa, $Pd_2(dba)_3$, Xantphos, DMF, 140 °C; (c) $R^2B(OH)_2$, KF, $[(tert\text{-}Bu)_3P]_2Pd(0)$, 1,4-dioxane, water, 120 °C; (d) NaI, AcCl, MeCN, 80 °C; (e) $R^2B(OH)_2$, KF, $[(tert\text{-}Bu)_3P]_2Pd(0)$, 1,4-dioxane, H_2O, 80 °C; (f) NaH, DMF, 0 °C; SEMCl, rt; (g) $(n\text{-}Bu)_3SnR^2$, LiCl, CuI, $Pd(PPh_3)_4$, 1,4-dioxane, 90 °C; (h) $R^2B(OH)_2$, $Pd(PPh_3)_4$, Cs_2CO_3, 1,4-dioxane, H_2O, 100 °C; (i) 1-Me-4-R^1-1*H*-pyrazol-3-amine, (*tert*-Bu)ONa, $Pd_2(dba)_3$, Xantphos, PhMe, 90 °C; (j) TBAF, Et_3N, THF, 70 °C.

CONCLUSIONS

A surrogate of the ATP binding site of the LRRK2 G2019S kinase domain derived from a 10-point mutant of checkpoint kinase 1 (CHK1 10-pt. mut.) was designed, expressed in insect cells infected with baculovirus and then purified and crystallized. Comparison of the binding affinity of 41 LRRK2 inhibitors with the mutant protein and their LRRK2 G2019S activity showed a moderate correlation between the two variables. X-ray crystal structures of the surrogate with known LRRK2 inhibitors rationalized their potency and selectivity, and its effectiveness was further demonstrated in the structure-guided optimization of a series of fragment-derived arylpyrrolo[2,3-*b*]-pyridines, leading to the discovery of selective LRRK2 inhibitors **22** and **23**.

In LRRK2-pSer935 HEK293 cell-based assays, the IC_{50} for compound **22** on LRRK2 WT, the overactive variant G2019S and the A2016T mutant was 24 nM, 40 nM and 471 nM, respectively. This confirmed that **22** is an inhibitor of LRRK2 WT and G2019S that engages Ala2016 in LRRK2, equivalent to Ala147 in the surrogate crystal structure.

Compound **22** was shown to be potent, selective, orally available and brain-penetrant in wild-type mice, and confirmation of target engagement was demonstrated with LRRK2-pSer935 IC_{50} values for **22** in mouse brain and kidney being 1.3 nM and 5 nM, respectively. Compound **23** and analogues had increased potency and selectivity for LRRK2, but had a pharmacokinetic profile unsuited to further progression as CNS drug candidates. Further work demonstrating the utility of the CHK1 10-pt. mut. crystallographic surrogate of the LRRK2 kinase domain in the optimization of other chemical series of inhibitors as potential treatments for Parkinson's disease will be published in due course.

EXPERIMENTAL SECTION

Expression and purification of CHK1 8, 10 and 12-point mutants. A clone representing the constitutively active CHK1 10-point mutant (N59L, V68I, L84M, Y86L, C87A, E91S, E134H, S147A, F149Y, G150S) was ordered from DNA2.0 Inc. (www.dna20.com), codon optimized for expression in baculovirus.

Bacmid generation using the pFastBac-1 vector was adopted as a cloning strategy with protein expression in *Spodoptera frugiperda* (Sf21) cells infected at 1e6/ml using a viral MOI = 3 and incubated at 27 °C, 120 rpm for 48 h.

The resulting cell pellet was re-suspended in lysis buffer (25 mM Tris-HCl pH 8.0, 0.5M NaCl, 20 mM imidazole, Roche EDTA free protease inhibitor cocktail, 4 mg/L DNase) and dounce homogenized using 20 strokes on ice. The homogenate was then centrifuged at 18,000 rpm for 90 min, 4 °C.

The clarified supernatant was loaded onto a 5 ml GE Healthcare chelating column charged with Ni^{2+} and pre-equilibrated in lysis buffer. The protein load was applied at 1 ml/min and the column then washed back to baseline with lysis buffer. The column was then eluted (lysis buffer pH 8.0 + 500 mM imidazole) at 2 ml/min over 20 CV with a linear gradient to 100% elution buffer. Fractions of interest were analyzed using SDS-PAGE and those containing the CHK1 10-pt. mutant protein were pooled and concentrated using Pierce 9K MWCO spin concentrators at 4 °C to achieve a size exclusion column load volume of <5% of the bed volume.

The concentrated pool was then applied at 1 ml/min onto a GE Healthcare Hiload 16/60 Superdex 75 pg size exclusion chromatography (SEC) column pre-equilibrated in SEC buffer (25 mM Tris-HCl pH 8.0, 0.5M NaCl, 5% glycerol, 5 mM DTT) and eluted with SEC buffer at 1 ml/min over 1.2 CV, collecting 0.5 ml fractions.

Samples of interest were analyzed by SDS-PAGE and the protein pool was concentrated using Pierce 9K MWCO spin concentrators at 4 °C.

The final protein yield was 0.5 mg/L culture volume at 1.9 mg/ml (58 μM), 95% purity. This was then snap frozen in a dry ice-methanol bath, prior to being stored at –80 °C.

The constitutively active 12 point mutant (A19S, Y20F, N59L, V68I, L84M, Y86L, C87A, E91S, E134H, S147A, F149Y, G150S) was also ordered from DNA2.0, codon optimized for expression in baculovirus. The 8 point mutant (N59L, V68I, L84M, Y86L, C87A, E91S, E134H, S147A) was generated retrospectively, with DNA being generated using site directed mutagenesis to back mutate two of the mutations in the 10 point mutant. Similar methodologies for gene cloning, protein expression and purification were used for each of the mutants produced.

CHK1 8, 10 and 12-point mutant crystallization. The CHK1 10-point mutant protein was thawed and concentrated to 19 mg/ml. Crystals were grown using the sitting drop vapor diffusion method at 20 °C. The protein was mixed with an equal volume of reservoir solution containing 7% (w/v) PEG 8000; 0.1M MES pH 6.5; 20% (v/v) ethylene glycol. Crystals appeared overnight.

Individual crystals were then harvested and transferred to a drop containing reservoir solution plus ligand at a final concentration of 2 mM. This was incubated at 20 °C overnight.

Soaked crystals were then briefly equilibrated in a cryoprotectant buffer containing reservoir solution plus 20% (v/v) glycerol and then flash frozen in liquid nitrogen.

Other mutants were crystallized and soaked in ligand solutions using an identical method.

Structures of complexes of CHK1 10 and 8-point mutants with **3b** were obtained by co-crystallization, where protein was mixed with compound (in molar ratio 1:4) prior to crystallization.

CHK1 8, 10 and 12-point mutant X-ray structure determination and refinement. Diffraction data were indexed and integrated using XDS[79] or SAINT[80] and SADABS[80] (CHK1 10-point mutant complex with **1**), scaled and truncated using XSCALE[79] or SCALA from the CCP4 suite of programs.[81] The structures were solved by molecular replacement with MolRep,[82] with the 1NVR[66] structure used as a starting model. All structures were refined using REFMAC,[83] and model building was done with Coot.[84] Topology files for the compounds were created by PRODRG[85] or AceDRG.[86]

LRRK2 WT and G2019S kinase activity assays. LRRK2 kinase activity was measured using a LanthaScreen kinase activity assay available from Invitrogen (ThermoFisher Scientific). GST-tagged truncated LRRK2 kinases were also obtained from Invitrogen (ThermoFisher Scientific), and comprised of residues 970 to 2527 of the full length human LRRK2 WT kinase (catalogue no. PV4874) or a similar sequence with the G2019S mutation (catalogue no. PV4882). The kinase reactions were performed in a 20 μL volume, in 384 well plates. The kinase reaction buffer consisted of 50 mM Tris pH 8.5, 0.01% polyoxyethylene (23) lauryl ether (BRIJ-35), 10 mM $MgCl_2$, 1 mM ethylene glycol-bis(β-aminoethyl ether)-*N,N,N′,N′*-tetraacetic acid (EGTA), and 2 mM DL-dithiothreitol (DTT).

In the assay, test compound (typically at 0 to 30 μM) was added to 1.3 mM ATP and 0.4 μM fluorescein-LRRKtide and then the kinase reaction was initiated by addition of either 1 nM LRRK2 WT or 250 pM LRRK2 G2019S kinase. The reaction mixture (20 μl total volume) was incubated for 2 hours at 30 °C before the reaction was terminated by addition of 10 mM EDTA and 1 nM terbium-labelled anti-phospho-LRRKtide antibody (final volume 40 μl). The mixture

was further incubated for 30 min at rt. TR-FRET was measured by excitation of the terbium-donor with 340 nm light and subsequent measurement (delay time 100 µs) of terbium and fluorescein emission at 495 nm and 520 nm respectively; over a time window of 1000 µs. TR-FRET measurements were performed on a Biomek Synergy Neo plate reader. The TR-FRET signal was calculated as the emission ratio at 520 nm over 495 nm. The TR-FRET ratio readout for test compounds was normalized to 0% inhibition, corresponding to TR-FRET ratio measured in control wells with no inhibition of the kinase activity and 100% inhibition, corresponding to TR-FRET ratio measured in control wells with 1 µM staurosporine. Test compound potency (IC_{50}) was estimated by nonlinear regression using the sigmoidal dose-response (variable slope) using Xlfit 4 (IDBS, Guildford, Surrey, UK, model 205). y = (A+((B-A)/(1+((C/x)^D)))), where y is the normalized TR-FRET ratio measurement for a given concentration of test compound, x is the concentration of test compound, A is the estimated efficacy (% inhibition) at infinite compound dilution, and B is the maximal efficacy (% inhibition). C is the IC_{50} value and D is the Hill slope coefficient. IC_{50} estimates were obtained from a minimum of 2 independent experiments and the logarithmic average was calculated.

K_i values were calculated as follows. $K_i = [I]_{50}/ ([L]_{50}/ K_D + [P]_0/ K_D + 1)$, where $[I]_{50}$ denotes the concentration of the free inhibitor at 50% inhibition, $[L]_{50}$ is the concentration of the free ligand (ATP) at 50% inhibition, $[P]_0$ is the concentration of the free protein at 0% inhibition, and K_D is the dissociation constant of the protein-ligand complex (ATP K_m for LRRK2 G2019S = 96 µM, ATP K_m for LRRK2 WT = 32 µM).

Ligand efficiency (LE) is defined as the free energy change (ΔG) associated with ligand binding per heavy atom, i.e. $LE = -\Delta G/ HAC = RT\ln K_i/ HAC$, where R = 0.001987 (gas constant in kcal/ mol/ K), T = 300 (temp in K) and HAC = heavy atom count.

LRRK2 pSer935 and pSer1292 kinase inhibition in LRRK2 WT, G2019S and A2016T expressing HEK293 cells. A cell-based quantitative immunocytochemistry LRRK2 mechanistic kinase inhibition assay based on LRRK2-Ser935 phosphorylation as the primary read-out was developed using the LI-COR Odyssey near infra-red technology, also denoted as In-Cell Western (ICW). The assay was performed in 96-well microplate format as previously described.[70] Additionally, the assay was performed in 384-well microplate format for LRRK2 WT and G2019S expressed in HEK293 cells. For the 384-well format assay, cells were transduced using BacMam technology (ThermoFisher Scientific). HEK293 cells were seeded in black, clear bottom 384-well cell-treated and poly-L-lysine-coated plates (Corning costar 3683) at a density of 20.000 cells/ well in 25 µl medium with 5% (v/v) BacMam LRRK2 WT or G2019S. The cells were incubated for 48 h before the assay was performed as previously described.[70] A LRRK2-Ser1292 phosphorylation assay was established for human LRRK2 G2019S, expressed by BacMam-transduced HEK293 cells grown in 384-well microplates as described for the LRRK2-pSer935 assay above. Phosphorylation of human LRRK2 Ser1292 was detected using rabbit anti-LRRK2-pSer1292 antibody diluted 1:800 (Epitomics).

Dosing of animals for *in vivo* studies. All animal experiments were carried out in in accordance with Danish law regulating experiments on animals, in compliance with EC directive 2010/63/EU, and the NIH guidelines on animal welfare. The protocol used for dosing of mice was approved by the institutional animal ethics committee. Compound **22** was administered by po dosing to 6–8 week old male C57BL/6 mice (Taconic Europe A/S) using 2-hydroxypropyl-β-cyclodextrin (25% w/v) as vehicle. A compound dosing range of 0.3–24 mg/kg was used and,

following 1 h of compound administration, brain hemispheres were snap frozen at -80 °C using dry ice. One brain hemisphere to be analyzed for LRRK2-pSer935 levels using either Western blotting or the LRRK2-pSer935 MSD immunoassay was homogenized (10% w/v) in a standard tissue homogenization buffer (ThermoFisher, cat. no. FNN0071). The other brain hemisphere was used to determine exposure of the compound. The experiment was performed three times (n = 3 male mice per treatment group per experiment; total n = 9 male mice per treatment group).

SDS-PAGE and Western blot-based determination of *in vivo* LRRK2-pSer935 inhibition. Brain and kidney samples were homogenized using Precellys lysing kit 0.5 ml (CK14 0.5 ml) in a cell lysis buffer (Sigma: C2978) with added protease (Roche: 11 697 498 011) and phosphatase inhibitors (Roche: 04 906 837 001). Total protein concentration was measured using a bicinchoninic acid (BCA) assay (ThermoFisher Pierce BCA protein assay kit, cat. no. 23225). Protein lysates were subjected to SDS-PAGE on a 3–8% Tris-Acetate gel (ThermoFisher NuPAGE^{TM} Tris-Acetate Mini Gels, cat. no. EA0375PK2) and transferred onto Immobilon-FL PVDF membranes (Merck Millipore, Billerica, MA, USA). After 1 h in blocking buffer, membranes were incubated overnight at 4 °C with primary antibodies diluted in blocking buffer: mouse monoclonal [N241A/34] anti-LRRK2 antibody (1:2000; NeuroMab, Davis, CA, USA) and rabbit monoclonal [UDD2 10(12)] anti-pS935-LRRK2 antibody (1:1000; RabMAb, Abcam, Cambridge, UK). Incubation with secondary antibodies was carried out for 1 h at rt: Anti-rabbit IgG F(c) (GOAT) antibody IRDye 800CW Conjugated (1:10,000; Rockland Immunochemicals Inc., Gilbertsville, USA) and anti-mouse Alexa Fluor 680 Goat anti-mouse IgM (1:20,000; ThermoFisher, UK). Protein visualization was detected using the LI-COR Odyssey CLx (LI-

COR, Nebraska, USA) and total LRRK2 and pSer935 band intensities were quantified using the LI-COR Odyssey software (Image Studio version 3.1.4).

In vivo **LRRK2-pSer935 MSD assay for IC_{50} determination of LRRK2 inhibitors**. Standard Meso Scale Diagnostics (MSD) Multi-array 96-well plates (Cat no: L15XA-3, MSD, Gaithersburg, Md, USA) were first coated with LRRK2 antibody (LRRK2-N241A/34, NeuroMab) at a concentration of 0.5 µg/ mL in 30 µL Tris-Base Saline (TBS). The plate was incubated over night at 4 °C without shaking. The plate was hereafter blocked by adding 150 µL 5% Blocker A (from MSD) and incubated at an orbital shaker (700 rpm) for 1.5 h at rt, followed by washing three times with 150 µL TBS including 0.05% Tween-20. Brain protein homogenates was diluted in TBS to a final concentration of 6.4 µg/ µl, and a volume of 25 µL (160 µg total protein) was added to each well in the MSD plate. Each individual protein lysate was added in duplicate for either pSer935-LRRK2 or total-LRRK2 measurement on either half of the plate. In one half of the plate, 25 µL (0.5 µg/ml) of the pSer935-LRRK2 antibody (Epitomics 5099-1) diluted in TBS including 0.05% Tween-20 and 1% Blocker A was added while 25 µL (0.5 µg/ml) of the LRRK2 antibody (MJFF3, Abcam) diluted in TBS including 0.05% Tween-20 and 1% Blocker A was added to the other half of the plate. The MJFF3 LRRK2 antibody and Epitomics pS935-LRRK2 antibody recognizes a different epitope compared to the LRRK2 antibody used in the coating thus allowing their binding and detection of the LRKK2 protein. The plates were incubated for one hour at room temperature with shaking at 700 rpm. The plate was hereafter washed three times with 150 µl per well of TBS including 0.05% Tween-20. The secondary anti Rabbit antibody, MSD SULFO-TAG conjugated, was added to the plate (25 µL/ well, 1 µg/ mL) and incubated at an orbital shaker (700 rpm) for 1 h at rt, followed by

three times washing with TBS including 0.05% Tween-20. After addition of 150 µL 2 × Read buffer (MSD) the plate was measured in the MSD SECTOR S 600. The raw data was analyzed using the default setting of the Discovery Workbench 4.0 software (MSD). For each sample, the signal derived from the pSer935-LRRK2 antibody was first normalized to the signal derived from the total-LRRK2 antibody and then expressed in percent of pSer935-LRRK2 of vehicle treated samples. IC_{50} values were determined by non-linear regression analysis using a sigmoidal variable slope curve fitting using the XLfit Excel add-in.

Chemistry. **General Methods**. All solvents and reagents were used as obtained from commercial vendors. ^{1}H NMR spectra were collected on Bruker spectrometers and chemical shifts are reported in ppm relative to the residual solvent peak. All tested compounds were determined to be >95% pure on HPLC chromatograms obtained on an Agilent 1290 Infinity II series instrument (see supplementary information for LC-MS method details). Purity was calculated as a percentage of total area at 254 nm. The mass spectra were obtained using the same instrument connected to an Agilent TOF 6230 single quadrupole with a ESI source. All active compounds were analyzed for and found to be free of pan assay interference compounds (PAINS).[87]

6-Amino-4-(3-methylphenyl)-1*H*-pyrrolo[2,3-*b*]pyridine-3-carbonitrile (22)

Step 1. Sodium hydride (15.12 g, 0.63 mol) was added to a solution of 4-chloro-1*H*-pyrrolo[2,3-*b*]pyridine-3-carbonitrile (**11**) (38.0 g, 0.21 mol) in DMF (750 mL) at 0 °C. After 10 min, 2-(trimethylsilyl)ethoxymethyl chloride (42.8 g, 0.25 mol) was added dropwise at 0 °C. After completion of addition, the reaction mixture was slowly warmed to rt. After 6 h, the reaction mixture was poured into ice-cold water and the resulting precipitate was filtered and

dried in vacuo. The material was subjected to silica-gel (100-200 mesh) column chromatography [EtOAc-petroleum ether 40-60 (5–10%) as eluent]. The eluted material, obtained as a white solid (48.6 g, 74%), was identified as 4-chloro-1-{[2-(trimethylsilyl)ethoxy]methyl}-1*H*-pyrrolo[2,3-*b*]pyridine-3-carbonitrile **37**; LC-MS (Method C) (*m/z*) 308 $[M + H]^+$; ^tR = 2.78 min. ^1H NMR ($CDCl_3$, 400 MHz) δ: 8.33 (1 H, d, *J* 5.6 Hz), 7.92 (1 H, s), 7.27 (1 H, d, *J* 5.2 Hz), 5.69 (2 H, s), 3.57 (2 H, t, *J* 8.4 Hz), 0.92 (2 H, t, *J* 8.4 Hz), -0.04 (9 H, s).

Step 2. Cesium carbonate (151 g, 0.47 mol) was added to a solution of **37** (48.0 g, 0.16 mol) and 3-phenylboronic acid (25.4 g, 0.19 mol) in 1,4-dioxane (1000 mL) and water (500 mL) at rt. The reaction mixture was degassed with argon for 30 min and then tetrakis(triphenylphosphine)palladium(0) (8.6 g, 0.0075 mol) was added. The reaction mixture was heated at 100 °C, with stirring. After 4 h, the reaction mixture was cooled to rt, diluted with ethyl acetate (2000 mL) and washed with water (1000 mL). The organic phase was washed with brine (1000 mL), dried (Na_2SO_4) and evaporated. The material was subjected to silica-gel (100-200 mesh) column chromatography [EtOAc-hexanes (5–10%) as eluent]. The eluted material, obtained as a yellow solid (39.2 g, 69%), was identified as 4-(3-methylphenyl)-1-{[2-(trimethylsilyl)ethoxy]methyl}-1*H*-pyrrolo[2,3-*b*]pyridine-3-carbonitrile **38**; LC-MS (Method F) (*m/z*) 364 $[M + H]^+$; ^tR = 1.47 min. ^1H NMR ($CDCl_3$, 400 MHz) δ: 8.47 (1 H, d, *J* 4.8 Hz), 7.94 (1 H, s), 7.45–7.40 (3 H, m), 7.31 (1 H, d, *J* 6.8 Hz), 7.25 (1 H,s), 5.74 (2 H, s), 3.61 (2 H, t, *J* 8.4 Hz), 2.47 (3 H, s), 0.94 (2 H, t, *J* 8.4 Hz), -0.04 (9 H, s).

Step 3. Triethylamine (59.8 mL, 0.43 mol) and TBAF (1M in THF, 429 mL, 0.43 mol) were added to a solution of **38** (39.0 g, 0.11 mol) in THF (200 mL) at rt. The reaction mixture was heated to 65 °C. After 16 h, the reaction was cooled to rt and evaporated. The residue was diluted with water (1000 mL) and the resulting precipitate was filtered and dried to a white solid (21.0 g,

84%), identified as 4-(3-methylphenyl)-1*H*-pyrrolo[2,3-*b*]pyridine-3-carbonitrile **18**, containing traces of TBAF; LC-MS (Method E) (*m/z*) 234 $[M + H]^+$; ^tR = 3.29 min. ^1H NMR (d_6-DMSO, 400 MHz) δ: 8.52 (1 H, d, *J* 2.0 Hz), 8.44 (1 H, d, *J* 4.8 Hz), 7.45–7.41 (3 H, m), 7.32–7.31 (1 H, m), 7.26 (1 H, d, *J* 4.8 Hz), 2.40 (3 H, s).

Step 4. *m*-CPBA (77%, 31.0 g, 0.18 mol) was added to a solution of **18** (21.0 g, 0.090 mol) in DCM (300 mL) at 0 °C. The reaction mixture was slowly warmed to rt. After 16 h, methanesulfonic acid (9.25 mL, 0.135 mol) was added, and the reaction mixture stirred at rt for 15 min. Diethyl ether (1 L) was added, and the resulting precipitate was then filtered and the residue dried to a white solid (23.69 g, 76%), identified as 3-cyano-4-(3-methylphenyl)-1*H*-pyrrolo[2,3-*b*]pyridin-7-ium-7-olate methylsulfonate salt **39**; LC-MS (Method C) (*m/z*) 250 $[M + H]^+$; ^tR = 1.76 min. ^1H NMR (d_6-DMSO, 400 MHz) δ: 8.49 (1 H, s), 8.37 (1 H, d, *J* 6.4 Hz), 7.44–7.40 (3 H, m), 7.31–7.29 (1 H, m), 7.26 (1 H, d, *J* 6.4 Hz), 2.39 (3 H, s), 2.32 (3 H, s).

Step 5. Methanesulfonyl chloride (23.15 g, 0.205 mol) was added to a solution of **39** (23.6 g, 0.068 mol) in DMF (500 mL) at rt. The reaction mixture was heated to 100 °C. After 2 h, the reaction mixture was cooled to rt, and poured onto ice-cold water (1000 mL). The resulting precipitate was filtered, and the residue dried to a white solid (17.2 g, 94%), identified as 6-chloro-4-(3-methylphenyl)-1*H*-pyrrolo[2,3-*b*]pyridine-3-carbonitrile **40**; LC-MS (Method C) (*m/z*) 268 $[M + H]^+$; ^tR = 2.39 min. ^1H NMR ($CDCl_3$, 400 MHz) δ: 10.74 (1 H, s), 7.94 (1 H, d, *J* 3.2 Hz), 7.45–7.40 (3 H, m), 7.35–7.33 (1 H, d, *J* 7.6 Hz), 7.30 (1 H, s), 2.48 (3 H, s).

Step 6. A mixture of **40** (20.0 g, 74.90 mmol) and LHMDS (1.0 M in THF, 300 mL, 300 mmol) in THF (400 mL) was degassed with argon for 10 min. 2-Dicyclohexylphosphino-2′,4′,6′-triisopropylbiphenyl (X-Phos, 3.56 g, 7.49 mmol) and tris(dibenzylideneacetone)dipalladium(0) (6.85 g, 7.49 mmol) were added and allowed to stir at 65 °C. After 16 h, the reaction mixture

was cooled to rt, 5N hydrochloric acid (300 mL) was added, and the reaction mixture stirred for 15 min. The mixture was then basified with sodium carbonate solution, extracted with ethyl acetate (2 × 500 mL) and the combined extracts dried (Na_2SO_4) and evaporated. The reside was subjected to silica-gel (100-200 mesh) column chromatography [ethyl acetate-petroleum ether 40-60 (20–30%)]. The eluted material was evaporated to a brown solid (14.2 g), which was further washed with diethyl ether (250 mL). The resulting brown solid (13.4 g, 72%) was identified as **22**; LC-MS (Method A) (*m/z*) 249 $[M + H]^+$; ^tR = 0.88 min. ^1H NMR (d_6-DMSO, 400 MHz) δ: 12.03 (1 H, s), 7.91 (1 H, d, *J* 2.8 Hz), 7.39–7.25 (4 H, m), 6.38 (1 H, s), 6.04 (1 H, s), 2.38 (3 H, s).

4-(3-Methylphenyl)-6-[(1-methylpyrazol-3-yl)amino]-1*H*-pyrrolo[2,3-*b*]pyridine-3-carbonitrile (23). *Step 1*. **11** (3.00 g, 16.89 mmol) was suspended in chloroform (60 mL) and the reaction mixture cooled to 0 °C. *m*-CPBA (10.3 g, 59.12 mmol) was then added portion-wise over 10 min and the reaction mixture was then stirred at rt for 16 h. Methanesulfonic acid (1.64 mL, 21.18 mmol) was then added drop-wise over 1 min. The reaction mixture was then diluted with diethyl ether (60 mL), cooled (ice-water bath) and then stirred for 30 min. The resulting precipitate was filtered, and the residue was washed with diethyl ether (3 × 20 mL). The resulting solid was dried *in vacuo* (60 °C) for 2 h to give 5.23 g (18.03 mmol, quantitative) of a beige solid, identified as 4-chloro-1*H*-pyrrolo[2,3-*b*]pyridine-3-carbonitrile-7-oxide methanesulfonic acid salt **35**; LC-MS (Method B) (*m/z*) 194 $[M + H]^+$; ^tR = 1.37 min. ^1H NMR (DMSO-d_6, 400 MHz) δ: 8.55 (1 H, s), 8.33 (1 H, d, *J* 6.7 Hz), 7.42 (1 H, d, *J* 6.7 Hz).

Step 2. **35** (5.37 g, 18.53 mmol) was suspended in DMF (50 mL). Methanesulfonyl chloride (10.87 g, 95 mmol) was then added, and the reaction mixture was then heated to 80 °C for 10 min, resulting in a pale-brown solution. The reaction mixture was then cooled and evaporated under reduced pressure. The resulting yellow gum was triturated with DCM. The precipitate was filtered and then dried to afford a light yellow powder (2.72 g, 8.52 mmol, 46%), identified as 4,6-dichloro-1*H*-pyrrolo[2,3-*b*]pyridine-3-carbonitrile **41**. LC-MS (Method B) (*m/z*) 210 $[M - H]^-$; ^tR = 2.27 min. ^1H NMR (DMSO-d_6, 400 MHz) δ: 13.37 (1 H, s), 8.61 (1 H, d, *J* 3.0 Hz), 7.64 (1 H, s).

Step 3. **41** (0.376 g, 1.77 mmol), 1-methyl-1*H*-pyrazol-3-amine (0.189 g, 1.95 mmol), sodium *tert*-butoxide (0.852 g, 8.87 mmol), tris(dibenzylideneacetone)dipalladium(0) (0.081 g, 0.090 mmol) and 4,5-bis(diphenylphosphino)-9,9-dimethylxanthene (Xantphos, 0.113 g, 0.20 mmol) were added to a microwave vial, followed by dry DMF (18 mL). The reaction mixture was flushed with N_2 for ~10 min, and then heated to 140 °C with microwaves for 1 h. The reaction mixture was filtered through Celite, and washed with ethyl acetate. The resulting precipitate was filtered and the residue dried and obtained as a yellow solid (0.242 g, 0.44 mmol, 50%) identified as 4-chloro-6-[(1-methyl-1*H*-pyrazol-3-yl)amino]-1*H*-pyrrolo[2,3-*b*]pyridine-3-carbonitrile (**42**). LC-MS (Method B) (*m/z*) 273 $[M + H]^+$; ^tR = 2.11 min. ^1H NMR (DMSO-d_6, 400 MHz) δ: 9.61 (1 H, s), 8.48 (1 H, s, br), 8.12 (1 H, s), 7.57 (1 H, d, *J* 2.2 Hz), 7.15 (1 H, s), 6.53 (1 H, d, *J* 2.3 Hz), 3.76 (3 H, s).

Step 4. **42** (0.234 g, 0.86 mmol), 3-methylphenylboronic acid (0.233 g, 1.72 mmol), potassium fluoride (0.150 g, 2.57 mmol), bis(tri-*tert*-butylphosphine)palladium(0) (0.005 g, 0.010 mmol) were suspended in 1,4-dioxane (15 mL) and water (2.5 mL) and stirred under a stream of nitrogen. The reaction mixture was then heated with microwaves at 120 °C for 60 min in a sealed

process vial. After cooling to room temperature, the reaction mixture was diluted with ethyl acetate and washed with brine. The organic phase was dried ($MgSO_4$) and concentrated *in vacuo*. The residue was subjected to silica-gel flash column chromatography [ethyl acetate-DCM (2:1) as eluent]. The eluted material, obtained as a white solid (0.068 g) underwent further purification by preparative HPLC to afford a white solid (0.047 g, 17%), identified as **23**; LC-MS (*m/z*) (Method A) 329 $[M + H]^+$; ^tR = 0.94 min. ^1H NMR (DMSO-d_6, 400 MHz) δ: 12.28 (1 H, s, br), 9.44 (1 H, s), 8.05–8.04 (1 H, d), 7.55–7.54 (1 H, d), 7.42–7.38 (2 H, m), 7.35–7.32 (1 H, m), 7.30–7.27 (1 H, m), 6.93 (1 H, s), 6.65–6.64 (1 H, d), 3.74 (3 H, s), 2.39 (3 H, s).

ASSOCIATED CONTENT

Supporting Information

Experimental details for compounds **12–21** and **24–34**, tables of X-ray data collection and refinement statistics, details of CHK1 WT and 10 point mutant kinase binding assays, table of LRRK2 G2019S activity and CHK1 WT and 10 point mutant kinase binding assay data, kinase selectivity data for compounds **22** and **23** and broad *in vitro* pharmacology profiling data for compound **23**.

Accession Codes

Authors will release the atomic coordinates upon article publication.

PDB codes for ligand bound structures with CHK1 8-pt. mut.: **2** (XXXX) and **3b** (XXXX).

PDB codes for ligand bound structures with CHK1 10-pt. mut.: γ-imino-ATP (XXXX), **1** (XXXX), **2** (XXXX), **3b** (XXXX), **4a** (XXXX), **5** (XXXX), **6** (XXXX), **7** (XXXX), **8** (XXXX), **9** (XXXX), **22** (XXXX) and **23** (XXXX).

PDB codes for ligand bound structures with CHK1 12-pt. mut.: **2** (XXXX) and **3b** (XXXX).

AUTHOR INFORMATION

Corresponding Author

*To whom correspondence should be addressed. E-mail: d.williamson@vernalis.com.

Phone: +44 (0) 1223 895555.

Author Contributions

The manuscript was written through contributions of all authors. All authors have given approval to the final version of the manuscript. The authors declare no competing financial interest.

ACKNOWLEDGMENT

The authors wish to thank Lassina Badolo for DMPK support, Jo Lerpiniere and Mandy Fallowfield for informatics support, Hayley Angove, Chris Pedder and Jalanie D'Alessandro for additional assay determinations, Loic Le Strat and Heather Simmonite for compound analytical support, James Taylor for assistance with compound sample management, Mike Wood for useful discussions and James Davidson for his assistance in the preparation of this manuscript.

ABBREVIATIONS USED

CHK1 10-pt. mut., 10-point mutant of checkpoint kinase 1; CL, clearance; ICW, In-Cell Western; LRRK2, leucine-rich repeat kinase 2; MDCK, Madin-Darby canine kidney; MLK1, mixed-lineage kinase; MDR1, Multi-Drug Resistance Gene; PBMC, peripheral blood mononuclear cell; SEM, 2-trimethylsilylethoxymethyl

REFERENCES

(1) Jankovic, J. Parkinson's Disease: Clinical Features and Diagnosis. *J. Neurol. Neurosurg. Psychiatry* **2008**, *79* (4), 368–376.

(2) Brundin, P.; Li, J.-Y.; Holton, J. L.; Lindvall, O.; Revesz, T. Research in Motion: The Enigma of Parkinson's Disease Pathology Spread. *Nat. Rev. Neurosci.* **2008**, *9* (10), 741–745.

(3) Poewe, W.; Mahlknecht, P.; Jankovic, J. Emerging Therapies for Parkinson's Disease. *Curr. Opin. Neurol.* **2012**, *25* (4), 448–459.

(4) Zhang, H.; Tong, R.; Bai, L.; Shi, J.; Ouyang, L. Emerging Targets and New Small Molecule Therapies in Parkinson's Disease Treatment. *Bioorg. Med. Chem.* **2016**, *24* (7), 1419–1430.

(5) Mills, R. D.; Mulhern, T. D.; Liu, F.; Culvenor, J. G.; Cheng, H. C. Prediction of the Repeat Domain Structures and Impact of Parkinsonism-Associated Variations on Structure and Function of All Functional Domains of Leucine-Rich Repeat Kinase 2 (LRRK2). *Hum. Mutat.* **2014**, *35* (4), 395–412.

(6) Tsika, E.; Moore, D. J. Contribution of GTPase Activity to LRRK2-Associated Parkinson

Disease. *Small GTPases* **2013**, *4* (3), 164–170.

(7) Gilsbach, B. K.; Kortholt, A. Structural Biology of the LRRK2 GTPase and Kinase Domains: Implications for Regulation. *Front. Mol. Neurosci.* **2014**, *7* (May), 32.

(8) Ray, S., Liu, M. Current Understanding of LRRK2 in Parkinson's Disease: Biochemical and Structural Features and Inhibitor Design. *Future Med. Chem.* **2012**, *4* (13), 1701–1713.

(9) Cookson, M. R. The Role of Leucine-Rich Repeat Kinase 2 (LRRK2) in Parkinson's Disease. *Nat. Rev. Neurosci.* **2010**, *11* (12), 791–797.

(10) Chan, S. L.; Angeles, D. C.; Tan, E.-K. Targeting Leucine-Rich Repeat Kinase 2 in Parkinson's Disease. *Expert Opin. Ther. Targets* **2013**, *17* (12), 1471–1482.

(11) Qing, H.; Wong, W.; McGeer, E. G.; McGeer, P. L. Lrrk2 Phosphorylates Alpha Synuclein at Serine 129: Parkinson Disease Implications. *Biochem. Biophys. Res. Commun.* **2009**, *387* (1), 149–152.

(12) Klein, C.; Westenberger, A. Genetics of Parkinson's Disease. *Cold Spring Harb. Perspect. Med.* **2012**, *2* (1), a008888.

(13) Trinh, J.; Amouri, R.; Duda, J. E.; Morley, J. F.; Read, M.; Donald, A.; Vilariño-Güell, C.; Thompson, C.; Szu Tu, C.; Gustavsson, E. K.; Ben Sassi, S.; Hentati, E.; Zouari, M.; Farhat, E.; Nabli, F.; Hentati, F.; Farrer, M. J. A Comparative Study of Parkinson's Disease and Leucine-Rich Repeat Kinase 2 p.G2019S Parkinsonism. *Neurobiol. Aging* **2014**, *35* (5), 1125–1131.

(14) Webber, P. J.; West, A. B. LRRK2 in Parkinson's Disease: Function in Cells and

Neurodegeneration. *FEBS J.* **2009**, *276* (22), 6436–6444.

(15) Zimprich, A.; Biskup, S.; Leitner, P.; Lichtner, P.; Farrer, M.; Lincoln, S.; Kachergus, J.; Hulihan, M.; Uitti, R. J.; Calne, D. B.; Stoessl, a. J.; Pfeiffer, R. F.; Patenge, N.; Carbajal, I. C.; Vieregge, P.; Asmus, F.; Müller-Myhsok, B.; Dickson, D. W.; Meitinger, T.; Strom, T. M.; Wszolek, Z. K.; Gasser, T. Mutations in LRRK2 Cause Autosomal-Dominant Parkinsonism with Pleomorphic Pathology. *Neuron* **2004**, *44* (4), 601–607.

(16) Albrecht, M. LRRK2 Mutations and Parkinsonism. *Lancet* **2005**, *365* (9466), 1230.

(17) Ramírez, M. B.; Pérez, J. M.; Rivero-Ríos, P.; Martínez-Salvador, M.; Lara Ordóñez, A. J.; Fernández, B.; Fdez, E.; Hilfiker, S. LRRK2 and Parkinson´s Disease: From Lack of Structure to Gain of Function. *Curr. Protein Pept. Sci.* **2016**, 1–10.

(18) West, A. B.; Moore, D. J.; Biskup, S.; Bugayenko, A.; Smith, W. W.; Ross, C. a; Dawson, V. L.; Dawson, T. M. Parkinson's Disease-Associated Mutations in Leucine-Rich Repeat Kinase 2 Augment Kinase Activity. *Proc. Natl. Acad. Sci. U. S. A.* **2005**, *102* (46), 16842–16847.

(19) Zhu, H.; Chen, H.; Cho, W.; Estrada, A. A.; Sweeney, Z. K. From Human Genetics to Drug Candidates: An Industrial Perspective on LRRK2 Inhibition as a Treatment for Parkinson's Disease. In *Medicinal Chemistry Approaches to Personalized Medicine*; Lackey, K., Roth, B. D., Eds.; Wiley-VCH Verlag GmbH & Co. KGaA., 2014; pp 227–254.

(20) Gilligan, P. J. Inhibitors of Leucine-rich Repeat Kinase 2 (LRRK2): Progress and Promise for the Treatment of Parkinson's Disease. *Curr. Top. Med. Chem.* **2015**, *15* (10), 928–938.

(21) Estrada, A. A.; Sweeney, Z. K. Chemical Biology of Leucine-Rich Repeat Kinase 2 (LRRK2) Inhibitors. *J. Med. Chem.* **2015**, *58* (17), 6733–6746.

(22) Ramsden, N.; Perrin, J.; Ren, Z.; Lee, B. D.; Zinn, N.; Dawson, V. L.; Tam, D.; Bova, M.; Lang, M.; Drewes, G.; Bantscheff, M.; Bard, F.; Dawson, T. M.; Hopf, C. Chemoproteomics-Based Design of Potent LRRK2-Selective Lead Compounds That Attenuate Parkinson's Disease-Related Toxicity in Human Neurons. *ACS Chem. Biol.* **2011**, *6* (10), 1021–1028.

(23) Kethiri, R. R.; Bakthavatchalam, R. Leucine-Rich Repeat Kinase 2 Inhibitors : A Review of Recent. *Expert Opin. Ther. Pat.* **2014**, *24* (7), 1–13.

(24) Galatsis, P. Leucine-Rich Repeat Kinase 2 Inhibitors: A Patent Review (2014-2016). *Expert Opin. Ther. Pat.* **2017**, 1–10.

(25) Schulz, S.; Ring, S. G.; Schmidt, B.; And, C.; Hopf, C. LRRK2 Kinase Inhibitors as New Drugs for Parkinson's Disease? In *RSC Drug Discovery Series No. 34: Emerging Drugs and Targets for Parkinson's Disease*; Martinez, A., Gil, C., Eds.; The Royal Society of Chemistry, 2013; pp 266–293.

(26) Kramer, T.; Lo Monte, F.; Göring, S.; Okala Amombo, G. M.; Schmidt, B. Small Molecule Kinase Inhibitors for LRRK2 and Their Application to Parkinson's Disease Models. *ACS Chem. Neurosci.* **2012**, *3* (3), 151–160.

(27) Kavanagh, M. E.; Doddareddy, M. R.; Kassiou, M. The Development of CNS-Active LRRK2 Inhibitors Using Property-Directed Optimisation. *Bioorganic Med. Chem. Lett.* **2013**, *23* (13), 3690–3696.

(28) Galatsis, P.; Henderson, J.; Kormos, B. L.; Hirst, W. D. Development of LRRK2 Kinase Inhibitors for Parkinson's Disease. In *Annual Reports in Medicinal Chemistry*; Desai, M. C., Ed.; Academic Press, 2014; Vol. 49, pp 43–58.

(29) Christensen, K. V.; Smith, G. P.; Williamson, D. S. Development of LRRK2 Inhibitors for the Treatment of Parkinson's Disease. In *Progress in Medicinal Chemistry*; Witty, D. R., Cox, B., Eds.; Elsevier, 2017; Vol. 56, pp 37–80.

(30) Hatcher, J. M.; Gray, N. S.; Choi, H. G.; Alessi, D. R. Small-Molecule Inhibitors of LRRK2. In *Leucine-Rich Repeat Kinase 2 (LRRK2), Advances in Neurobiology*; Rideout, H. J., Ed.; Springer, 2017; Vol. 14, pp 241–264.

(31) Covy, J. P.; Giasson, B. I. Identification of Compounds That Inhibit the Kinase Activity of Leucine-Rich Repeat Kinase 2. *Biochem. Biophys. Res. Commun.* **2009**, *378* (3), 473–477.

(32) Deng, X.; Dzamko, N.; Prescott, A.; Davies, P.; Liu, Q.; Yang, Q.; Lee, J.-D.; Patricelli, M. P.; Nomanbhoy, T. K.; Alessi, D. R.; Gray, N. S. Characterization of a Selective Inhibitor of the Parkinson's Disease Kinase LRRK2. *Nat. Chem. Biol.* **2011**, *7* (4), 203–205.

(33) Reith, A. D.; Bamborough, P.; Jandu, K.; Andreotti, D.; Mensah, L.; Dossang, P.; Choi, H. G.; Deng, X.; Zhang, J.; Alessi, D. R.; Gray, N. S. GSK2578215A; A Potent and Highly Selective 2-Arylmethyloxy-5-Substitutent-N-Arylbenzamide LRRK2 Kinase Inhibitor. *Bioorg. Med. Chem. Lett.* **2012**, *22* (17), 5625–5629.

(34) Estrada, A. a.; Liu, X.; Baker-Glenn, C.; Beresford, A.; Burdick, D. J.; Chambers, M.; Chan, B. K.; Chen, H.; Ding, X.; Dipasquale, A. G.; Dominguez, S. L.; Dotson, J.;

Drummond, J.; Flagella, M.; Flynn, S.; Fuji, R.; Gill, A.; Gunzner-Toste, J.; Harris, S. F.; Heffron, T. P.; Kleinheinz, T.; Lee, D. W.; Le Pichon, C. E.; Lyssikatos, J. P.; Medhurst, A. D.; Moffat, J. G.; Mukund, S.; Nash, K.; Scearce-Levie, K.; Sheng, Z.; Shore, D. G.; Tran, T.; Trivedi, N.; Wang, S.; Zhang, S.; Zhang, X.; Zhao, G.; Zhu, H.; Sweeney, Z. K. Discovery of Highly Potent, Selective, and Brain-Penetrable Leucine-Rich Repeat Kinase 2 (LRRK2) Small Molecule Inhibitors. *J. Med. Chem.* **2012**, *55* (22), 9416–9433.

(35) Henderson, J. L.; Kormos, B. L.; Hayward, M. M.; Coffman, K. J.; Jasti, J.; Kurumbail, R. G.; Wager, T. T.; Verhoest, P. R.; Noell, G. S.; Chen, Y.; Needle, E.; Berger, Z.; Steyn, S. J.; Houle, C.; Hirst, W. D.; Galatsis, P. Discovery and Preclinical Profiling of 3-[4-(Morpholin-4-Yl)-7H-pyrrolo[2,3-D]pyrimidin-5-Yl]benzonitrile (PF-06447475), a Highly Potent, Selective, Brain Penetrant, and in Vivo Active LRRK2 Kinase Inhibitor. *J. Med. Chem.* **2015**, *58* (1), 419–432.

(36) Hatcher, J. M.; Zhang, J.; Geun, H.; Ito, G.; Alessi, D. R.; Choi, H. G.; Ito, G.; Alessi, D. R.; Gray, N. S. Discovery of a Pyrrolopyrimidine (JH-II-127), a Highly Potent , Selective and Brain Penetrant LRRK2 Inhibitor. *ACS Med. Chem. Lett.* **2015**, *6*, 584–589.

(37) Fell, M. J.; Mirescu, C.; Basu, K.; Cheewatrakoolpong, B.; DeMong, D. E.; Ellis, J. M.; Hyde, L. A.; Lin, Y.; Markgraf, C. G.; Mei, H.; Miller, M.; Poulet, F. M.; Scott, J. D.; Smith, M. D.; Yin, Z.; Zhou, X.; Parker, E. M.; Kennedy, M. E.; Morrow, J. A. MLi-2, a Potent, Selective, and Centrally Active Compound for Exploring the Therapeutic Potential and Safety of LRRK2 Kinase Inhibition. *J. Pharmacol. Exp. Ther.* **2015**, *355* (3), 397–409.

(38) Scott, J. D.; DeMong, D. E.; Greshock, T. J.; Basu, K.; Dai, X.; Harris, J.; Hruza, A.; Li,

S. W.; Lin, S.-I.; Liu, H.; Macala, M. K.; Hu, Z.; Mei, H.; Zhang, H.; Walsh, P.; Poirier, M.; Shi, Z.; Xiao, L.; Agnihotri, G.; Baptista, M. A. S.; Columbus, J.; Fell, M. J.; Hyde, L. A.; Kuvelkar, R.; Lin, Y.; Mirescu, C.; Morrow, J. A.; Yin, Z.; Zhang, X.; Zhou, X.; Chang, R. K.; Embrey, M. W.; Sanders, J. M.; Tiscia, H. E.; Drolet, R. E.; Kern, J. T.; Sur, S. M.; Renger, J. J.; Bilodeau, M. T.; Kennedy, M. E.; Parker, E. M.; Stamford, A. W.; Nargund, R. P.; McCauley, J. A.; Miller, M. W. Discovery of a 3-(4-Pyrimidinyl) Indazole (MLi-2), an Orally Available and Selective Leucine-Rich Repeat Kinase 2 (LRRK2) Inhibitor That Reduces Brain Kinase Activity. *J. Med. Chem.* **2017**, *60* (7), 2983–2992.

(39) Smith, G. P.; Badolo, L.; Chell, V.; Chen, I.-J.; Christensen, K. V.; David, L.; Daechsel, J. A.; Hentzer, M.; Herzig, M. C.; Mikkelsen, G. K.; Watson, S. P.; Williamson, D. S. The Design and SAR of a Novel Series of 2-Aminopyridine Based LRRK2 Inhibitors. *Bioorganic Med. Chem. Lett.* **2017**, https://doi.org/10.1016/j.bmcl.2017.07.072.

(40) Fuji, R. N.; Flagella, M.; Baca, M.; S Baptista, M. A.; Brodbeck, J.; Chan, B. K.; Fiske, B. K.; Honigberg, L.; Jubb, A. M.; Katavolos, P.; Lee, D. W.; Lewin-Koh, S.-C.; Lin, T.; Liu, X.; Liu, S.; Lyssikatos, J. P.; O'Mahony, J.; Reichelt, M.; Roose-Girma, M.; Sheng, Z.; Sherer, T.; Smith, A.; Solon, M.; Sweeney, Z. K.; Tarrant, J.; Urkowitz, A.; Warming, S.; Yaylaoglu, M.; Zhang, S.; Zhu, H.; Estrada, A. A.; Watts, R. J. Effect of Selective LRRK2 Kinase Inhibition on Nonhuman Primate Lung. *Sci. Transl. Med.* **2015**, *7* (273), 273ra15.

(41) Taymans, J.-M.; Greggio, E. LRRK2 Kinase Inhibition as a Therapeutic Strategy for Parkinson's Disease, Where Do We Stand? *Curr. Neuropharmacol.* **2016**, *14* (3), 214–

225.

(42) Liu, Z.; Galemmo, R. A.; Fraser, K. B.; Moehle, M. S.; Sen, S.; Volpicelli-Daley, L. A.; DeLucas, L. J.; Ross, L. J.; Valiyaveettil, J.; Moukha-Chafiq, O.; Pathak, A. K.; Ananthan, S.; Kezar, H.; White, E. L.; Gupta, V.; Maddry, J. a.; Suto, M. J.; West, A. B. Unique Functional and Structural Properties of the LRRK2 Protein ATP-Binding Pocket. *J. Biol. Chem.* **2014**, *289* (47), 32937–32951.

(43) Zhang, J.; Deng, X.; Choi, H. G.; Alessi, D. R.; Gray, N. S. Characterization of TAE684 as a Potent LRRK2 Kinase Inhibitor. *Bioorganic Med. Chem. Lett.* **2012**, *22* (5), 1864–1869.

(44) Choi, H. G.; Zhang, J.; Deng, X.; Hatcher, J. M.; Patricelli, M. P.; Zhao, Z.; Alessi, D. R.; Gray, N. S. Brain Penetrant LRRK2 Inhibitor. *ACS Med. Chem. Lett.* **2012**, *3* (8), 658–662.

(45) Liu, M.; Kang, S.; Ray, S. S.; Jackson, J.; Zaitsev, A. D.; Gerber, S. a; Cuny, G. D.; Glicksman, M. a. Kinetic Mechanistic and Structural Modeling Studies of Truncated Wild-Type LRRK2 and the Mutant G2019S. *Biochemistry* **2011**, *50*, 9399–9408.

(46) Göring, S.; Taymans, J.-M.; Baekelandt, V.; Schmidt, B. Indolinone Based LRRK2 Kinase Inhibitors with a Key Hydrogen Bond. *Bioorg. Med. Chem. Lett.* **2014**, *24* (19), 4630–4637.

(47) Liu, M.; Bender, S. A.; Cuny, G. D.; Sherman, W.; Glicksman, M.; Ray, S. S. Type II Kinase Inhibitors Show an Unexpected Inhibition Mode against Parkinson's Disease-Linked LRRK2 Mutant G2019S. *Biochemistry* **2013**, *52* (10), 1725–1736.

(48) Gancia, E.; De Groot, M.; Burton, B.; Clark, D. E. Discovery of LRRK2 Inhibitors by Using an Ensemble of Virtual Screening Methods. *Bioorg. Med. Chem. Lett.* **2017**, http://dx.doi.org/10.1016/j.bmcl.2017.03.098.

(49) Chen, H.; Chan, B. K.; Drummond, J.; Estrada, A. A.; Gunzner-Toste, J.; Liu, X.; Liu, Y.; Moffat, J.; Shore, D.; Sweeney, Z. K.; Tran, T.; Wang, S.; Zhao, G.; Zhu, H.; Burdick, D. J. Discovery of Selective LRRK2 Inhibitors Guided by Computational Analysis and Molecular Modeling. *J. Med. Chem.* **2012**, *55* (11), 5536–5545.

(50) Lang, C. A.; Ray, S. S.; Liu, M.; Singh, A. K.; Cuny, G. D. Discovery of LRRK2 Inhibitors Using Sequential in Silico Joint Pharmacophore Space (JPS) and Ensemble Docking. *Bioorganic Med. Chem. Lett.* **2015**, *25* (13), 2713–2719.

(51) Chan, B. K.; Estrada, A. a.; Chen, H.; Atherall, J.; Baker-Glenn, C.; Beresford, A.; Burdick, D. J.; Chambers, M.; Dominguez, S. L.; Drummond, J.; Gill, A.; Kleinheinz, T.; Le Pichon, C. E.; Medhurst, A. D.; Liu, X.; Moffat, J. G.; Nash, K.; Scearce-Levie, K.; Sheng, Z.; Shore, D. G.; Van De Poël, H.; Zhang, S.; Zhu, H.; Sweeney, Z. K. Discovery of a Highly Selective, Brain-Penetrant Aminopyrazole LRRK2 Inhibitor. *ACS Med. Chem. Lett.* **2013**, *4* (1), 85–90.

(52) Troxler, T.; Greenidge, P.; Zimmermann, K.; Desrayaud, S.; Drückes, P.; Schweizer, T.; Stauffer, D.; Rovelli, G.; Shimshek, D. R. Discovery of Novel Indolinone-Based, Potent, Selective and Brain Penetrant Inhibitors of LRRK2. *Bioorganic Med. Chem. Lett.* **2013**, *23* (14), 4085–4090.

(53) Munoz, L.; Kavanagh, M. E.; Phoa, A. F.; Heng, B.; Dzamko, N.; Chen, E.-J.; Doddareddy, M. R.; Guillemin, G. J.; Kassiou, M. Optimisation of LRRK2 Inhibitors and

Assessment of Functional Efficacy in Cell-Based Models of Neuroinflammation. *Eur. J. Med. Chem.* **2015**, *95*, 29–34.

(54) Garofalo, A. W.; Adler, M.; Aubele, D. L.; Brigham, E. F.; Chian, D.; Franzini, M.; Goldbach, E.; Kwong, G. T.; Motter, R.; Probst, G. D.; Quinn, K. P.; Ruslim, L.; Sham, H. L.; Tam, D.; Tanaka, P.; Truong, A. P.; Ye, X. M.; Ren, Z. Discovery of 4-Alkylamino-7-Aryl-3-Cyanoquinoline LRRK2 Kinase Inhibitors. *Bioorganic Med. Chem. Lett.* **2013**, *23* (7), 1974–1977.

(55) Franzini, M.; Ye, X. M.; Adler, M.; Aubele, D. L.; Garofalo, A. W.; Gauby, S.; Goldbach, E.; Probst, G. D.; Quinn, K. P.; Santiago, P.; Sham, H. L.; Tam, D.; Truong, A.; Ren, Z. Triazolopyridazine LRRK2 Kinase Inhibitors. *Bioorganic Med. Chem. Lett.* **2013**, *23* (7), 1967–1973.

(56) Nichols, R. Jeremy; Dzamko, Nicolas ; Hutti, Jessica E.; Cantley, Lewis C.; Deak, Maria; Moran, Jennifer; Bamborough, Paul ; Reith, Alastair D. and Alessi, D. R. Substrate Specificity and Inhibitors of LRRK2, a Protein Kinase Mutated in Parkinson's Disease. *Biochem. J.* **2009**, *60*, 47–60.

(57) Yun, H.; Heo, H. Y.; Kim, H. H.; DooKim, N.; Seol, W. Identification of Chemicals to Inhibit the Kinase Activity of Leucine-Rich Repeat Kinase 2 (LRRK2), a Parkinson's Disease-Associated Protein. *Bioorganic Med. Chem. Lett.* **2011**, *21* (10), 2953–2957.

(58) Greshock, T. J.; Sanders, J. M.; Drolet, R. E.; Rajapakse, H. A.; Chang, R. K.; Kim, B.; Rada, V. L.; Tiscia, H. E.; Su, H.; Lai, M.-T.; Sur, S. M.; Sanchez, R. I.; Bilodeau, M. T.; Renger, J. J.; Kern, J. T.; McCauley, J. A. Potent, Selective and Orally Bioavailable Leucine-Rich Repeat Kinase 2 (LRRK2) Inhibitors. *Bioorg. Med. Chem. Lett.* **2016**, *26*

(11), 2631–2635.

(59) Galatsis, P.; Henderson, J. L.; Kormos, B. L.; Han, S.; Kurumbail, R. G.; Wager, T. T.; Verhoest, P. R.; Noell, G. S.; Chen, Y.; Needle, E.; Berger, Z.; Steyn, S. J.; Houle, C.; Hirst, W. D. Kinase Domain Inhibition of Leucine Rich Repeat Kinase 2 (LRRK2) Using a [1,2,4]triazolo[4,3-B]pyridazine Scaffold. *Bioorganic Med. Chem. Lett.* **2014**, *24* (17), 4132–4140.

(60) Gilsbach, B. K.; Ho, F. Y.; Vetter, I. R.; van Haastert, P. J. M.; Wittinghofer, a.; Kortholt, a. Roco Kinase Structures Give Insights into the Mechanism of Parkinson Disease-Related Leucine-Rich-Repeat Kinase 2 Mutations. *Proc. Natl. Acad. Sci.* **2012**, *109* (26), 10322–10327.

(61) Gilsbach, B. K.; Messias, A. C.; Ito, G.; Sattler, M.; Alessi, D. R.; Wittinghofer, A.; Kortholt, A. Structural Characterization of LRRK2 Inhibitors. *J. Med. Chem.* **2015**, *58* (9), 3751–3756.

(62) Berman, H. M.; Westbrook, J.; Feng, Z.; Gilliland, G.; Bhat, T. N.; Weissig, H.; Shindyalov, I. N.; Bourne, P. E. The Protein Data Bank. *Nucleic Acids Res.* **2000**, *28* (1), 235–242.

(63) Hudkins, R. L.; Diebold, J. L.; Tao, M.; Josef, K. A.; Park, C. H.; Angeles, T. S.; Aimone, L. D.; Husten, J.; Ator, M. A.; Meyer, S. L.; Holskin, B. P.; Durkin, J. T.; Fedorov, A. A.; Fedorov, E. V.; Almo, S. C.; Mathiasen, J. R.; Bozyczko-Coyne, D.; Saporito, M. S.; Scott, R. W.; Mallamo, J. P. Mixed-Lineage Kinase 1 and Mixed-Lineage Kinase 3 Subtype-Selective Dihydronaphthyl[3,4-a]pyrrolo[3,4-C]carbazole-5-Ones: Optimization, Mixed-Lineage Kinase 1 Crystallography, and Oral in Vivo Activity in 1-Methyl-4-

Phenyltetrahydropyridine Models. *J. Med. Chem.* **2008**, *51*, 5680–5689.

(64) Massey, A. J.; Stokes, S.; Browne, H.; Foloppe, N.; Fiumana, A.; Scrace, S.; Fallowfield, M.; Bedford, S.; Webb, P.; Baker, L.; Christie, M.; Drysdale, M. J.; Wood, M. Identification of Novel, in Vivo Active Chk1 Inhibitors Utilizing Structure Guided Drug Design. *Oncotarget* **2015**, *6* (34), 35797–35812.

(65) Foloppe, N.; Fisher, L. M.; Howes, R.; Kierstan, P.; Potter, A.; Robertson, A. G. S.; Surgenor, A. E. Structure-Based Design of Novel Chk1 Inhibitors: Insights into Hydrogen Bonding and Protein-Ligand Affinity. *J. Med. Chem.* **2005**, *48* (13), 4332–4345.

(66) Zhao, B.; Bower, M. J.; McDevitt, P. J.; Zhao, H.; Davis, S. T.; Johanson, K. O.; Green, S. M.; Concha, N. O.; Zhou, B. B. S. Structural Basis for Chk1 Inhibition by UCN-01. *J. Biol. Chem.* **2002**, *277* (48), 46609–46615.

(67) Schrödinger LLC. *The PyMOL Molecular Graphics System, Version 1.8*.

(68) Greshock, T. J.; Sanders, J. M.; Drolet, R. E.; Rajapakse, H. A.; Chang, R. K.; Kim, B.; Rada, V. L.; Tiscia, H. E.; Su, H.; Lai, M.-T.; Sur, S. M.; Sanchez, R. I.; Bilodeau, M. T.; Renger, J. J.; Kern, J. T.; McCauley, J. A. Potent, Selective and Orally Bioavailable Leucine-Rich Repeat Kinase 2 (LRRK2) Inhibitors. *Bioorg. Med. Chem. Lett.* **2016**, *26* (11), 2631–2635.

(69) Nichols, P. L.; Eatherton, A. J.; Bamborough, P.; Jandu, K. S.; Philps, O. J.; Andreotti, D. Novel Compounds. WO 2011/038572, 2011.

(70) Afsari, F.; Christensen, K. V.; Smith, G. P.; Hentzer, M.; Nippe, O. M.; Elliott, C. J. H.; Wade, A. R. Abnormal Visual Gain Control in a Parkinson's Disease Model. *Hum. Mol.*

Genet. **2014**, *23* (17), 4465–4478.

(71) Ding, X.; Liu, Q.; Sang, Y.; Stasi, L. P.; Wan, Z.; Zhao, B.; Edge, C. M. Compounds. WO 2015/113452, 2015.

(72) Galatsis, P.; Hayward, M. M.; Kormos, B. L.; Wager, T. T.; Zhang, L.; Henderson, J. L.; Kurumbail, R. G.; Verhoest, P. R.; Stepan, A. F. Novel 3,4-Disubstituted 1H-pyrrolo[2,3-B]pyridines and 4,5-Disubstiuted -7H-pyrrolo[2,3-C]pyridazines as LRRK2 Inhibitors. WO 2015/092592, 2015.

(73) Brough, P.; Drysdale, M. 1H-Pyrrolo[2,3-B]pyridine Derivatives Useful as Hsp90 Inhibitors. WO 2008/025947, 2008.

(74) Nikolovska-Coleska, Z.; Wang, R.; Fang, X.; Pan, H.; Tomita, Y.; Li, P.; Roller, P. P.; Krajewski, K.; Saito, N. G.; Stuckey, J. A.; Wang, S. Development and Optimization of a Binding Assay for the XIAP BIR3 Domain Using Fluorescence Polarization. *Anal. Biochem.* **2004**, *332* (2), 261–273.

(75) Hopkins, A. L.; Groom, C. R.; Alex, A. Ligand Efficiency: A Useful Metric for Lead Selection. *Drug Discov. Today* **2004**, *9* (10), 430–431.

(76) Bedford, S. T.; Chen, I.-J.; Wang, Y.; Williamson, D. S. Arylpyrrolopyridine Derived Compounds as LRRK2 Inhibitors. US 2017/0020850, 2017.

(77) Nichols, R. J. LRRK2 Phosphorylation. In *Leucine-Rich Repeat Kinase 2 (LRRK2), Advances in Neurobiology*; Rideout, H. J., Ed.; Springer, 2017; pp 51–70.

(78) Graves, L. M.; Litchfield, D. W. "Going KiNativ": Probing the Native Kinome. *Chem. Biol.* **2011**, *18* (6), 683–684.

(79) Kabsch, W. Software XDS for Image Rotation, Recognition and Crystal Symmetry Assignment. *Acta Crystallogr. Sect. D Biol. Crystallogr.* **2010**, *66* (2), 125–132.

(80) SAINT. Bruker AXS: Madison, Wisconsin, USA 2015.

(81) Winn, M. D.; Ballard, C. C.; Cowtan, K. D.; Dodson, E. J.; Emsley, P.; Evans, P. R.; Keegan, R. M.; Krissinel, E. B.; Leslie, A. G. W.; McCoy, A.; McNicholas, S. J.; Murshudov, G. N.; Pannu, N. S.; Potterton, E. A.; Powell, H. R.; Read, R. J.; Vagin, A.; Wilson, K. S. Overview of the CCP4 Suite and Current Developments. *Acta Crystallogr. Sect. D Biol. Crystallogr.* **2011**, *67* (4), 235–242.

(82) Vagin, A.; Teplyakov, A. MOLREP: An Automated Program for Molecular Replacement. *J. Appl. Crystallogr.* **1997**, *30* (6), 1022–1025.

(83) Murshudov, G. N.; Skubak, P.; Lebedev, A. A.; Pannu, N. S.; Steiner, R. A.; Nicholls, R. A.; Winn, M. D.; Long, F.; Vagin, A. A. REFMAC5 for the Refinement of Macromolecular Crystal Structures. *Acta Crystallogr. Sect. D Biol. Crystallogr.* **2011**, *67* (4), 355–367.

(84) Emsley, P.; Lohkamp, B.; Scott, W. G.; Cowtan, K. Features and Development of Coot. *Acta Crystallogr. Sect. D Biol. Crystallogr.* **2010**, *66* (4), 486–501.

(85) Schuttelkopf, A. W.; van, A. D. M. F. PRODRG: A Tool for High-Throughput Crystallography of Protein-Ligand Complexes. *Acta Crystallogr. D. Biol. Crystallogr.* **2004**, *60* (Pt 8), 1355–1363.

(86) Long, F.; Nicholls, R. A.; Emsley, P.; Grazulis, S.; Merkys, A.; Vaitkus, A.; Murshudov, G. N. AceDRG: A Stereochemical Description Generator for Ligands. *Acta Crystallogr.*

Sect. D Struct. Biol. **2017**, *73* (2), 112–122.

(87) Baell, J. B.; Holloway, G. A. New Substructure Filters for Removal of Pan Assay Interference Compounds (PAINS) from Screening Libraries and for Their Exclusion in Bioassays. *J. Med. Chem.* **2010**, *53* (7), 2719–2740.

TABLE OF CONTENTS GRAPHIC

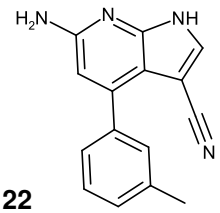

Compd **22**

LRRK2 Variant	**LRRK2-pSer935 HEK293 IC_{50} (nM)**
WT	24
G2019S	40
A2016T	471

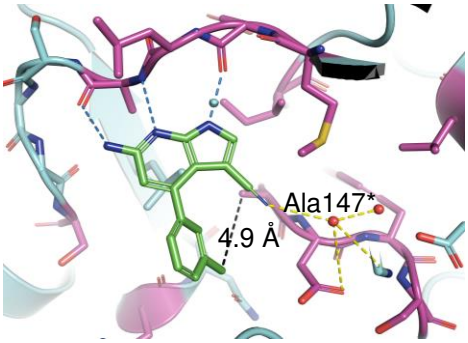

X-ray **22**/ CHK1 10-pt. mut.
*(Ala2016 in LRRK2)